Retrieval of macro- and micro-physical properties of oceanic hydrosols from polarimetric observations

Amir Ibrahim[1,2,3,*], Alexander Gilerson[1], Jacek Chowdhary[4,5], and Samir Ahmed[1]

[1]Optical Remote Sensing Laboratory, Department of Electrical Engineering, The City College of the City University of New York, New York, New York 10031, USA, [2]NASA Goddard Space Flight Center, Greenbelt, Maryland 20771, USA, [3]Universities Space Research Association, Columbia, Maryland 21044, USA, [4]Department of Applied Physics and Applied Mathematics, Columbia University, New York, New York 10025, USA, [5]NASA Goddard Institute for Space Studies, New York, New York 10025, USA

**amir.ibrahim@nasa.gov*

Abstract

Remote sensing has mainly relied on measurements of scalar radiance and its spectral and angular features to retrieve micro- and macro- physical properties of aerosols/hydrosols. However, it is recognized that measurements that include the polarimetric characteristics of light provide more intrinsic information about particulate scattering. To take advantage of this, we used vector radiative transfer (VRT) simulations and developed an analytical relationship to retrieve the macro and micro- physical properties of the oceanic hydrosols. Specifically, we investigated the relationship between the observed degree of linear polarization (DoLP) and the ratio of attenuation-to-absorption coefficients (c/a) in water, from which the scattering coefficient can be readily computed ($b = c - a$), after retrieving a. This relationship was parameterized for various scattering geometries, including sensor zenith/azimuth angles relative to the Sun's principal plane, and for varying Sun zenith angles. An inversion method was also developed for the retrieval of the microphysical properties of hydrosols, such as the bulk refractive index and the particle size distribution. The DoLP vs *c*/*a* relationship was tested and validated against in-situ measurements of underwater light polarization obtained by a custom-built polarimeter and measurements of the coefficients *a* and *c,* obtained using an in-water WET Labs ac-s instrument package. These measurements confirmed the validity of the approach, with retrievals of attenuation coefficients showing a high coefficient of determination depending on the wavelength. We also performed a sensitivity analysis of the DoLP at the Top of Atmosphere (TOA) over coastal waters showing the possibility of polarimetric remote sensing application for ocean color.

1. Introduction

The polarization of light is highly sensitive to chemical and physical properties of particles in the atmosphere and oceans (Hansen and Travis 1974, Kattawar and Adams 1989, Mishchenko, Cairns et al. 2004, Chami and Platel 2007, Lotsberg and Stamnes 2010, Knobelspiesse, Cairns et al. 2011, Chowdhary, Cairns et al. 2012). The development of satellite sensors capable of measuring and quantifying the polarization of light emerging from atmosphere-ocean (AO) system is becoming increasingly important for understanding not only the macrophysics, but also the microphysics of particulate matter in AO system. The microphysical properties reveal new details about aerosol/hydrosol characteristics that make it possible to distinguish between different aerosol/hydrosol types from space observations, and to derive precise distributions of size, shape, and concentrations that can help in our understanding of the earth's radiation budget, climate change, and ocean processes (Hansen and Travis 1974, Chowdhary, Cairns et al. 2006, Chowdhary, Cairns et al. 2012). Consequently, NASA is considering the addition of a polarimeter onboard a future ocean color mission: the Plankton, Aerosol, Cloud, and Ocean Ecosystem (PACE) (PACE 2012). The long-term goal of this mission is essentially to assess the carbon cycle and its interrelationship with climate change. It also will extend the ocean climate data records collected since the 1990s and evaluate observed long-term changes. Polarimetric measurements from space will improve atmospheric corrections, especially over bright coastal and shallow waters (Chowdhary 1999, Chowdhary, Cairns et al. 2001, Waquet, Cairns et al. 2009, Knobelspiesse, Cairns et al. 2011). While polarization and multi-angle measurements can be used to derive some key properties of aerosols, such measurements can also be useful in retrieving the optical and microphysical oceanic properties (PACE 2012). In addition, the planned Multiviewing, Multichannel, and Multipolarization Imager - 3MI (ESA/Eumetsat) will help with understanding the composition of aerosols and clouds in the atmosphere and possibly the oceanic hydrosols and their impact on climate forcing (Marbach, Riedi et al. 2015). The Second Generation Global Imager (SGLI) on-board the Japanese Global Change Observation Mission (GCOM-C) will provide atmosphere, land, and ocean color products. The two added polarization channels with 250-meter spatial resolution will help to improve aerosol and ocean color retrievals, especially in coastal regions (Honda, Yamamoto et al. 2006). The studies and analyses performed in this work will contribute to the development of comprehensive remote sensing inversion algorithms that utilize the polarimetric signature of the ocean for the retrieval of macro- and micro-physical properties of hydrosols.

Several studies have shown the potential of utilizing the polarization characteristics of oceanic light to retrieve Inherent Optical Properties (IOPs) and biogeochemical properties (Chami, Santer et al. 2001, Chami and Mckee 2007, Chami and Platel 2007, Loisel, Duforet et al. 2008, Lotsberg and Stamnes 2010, Tonizzo, Gilerson et al. 2011, Ibrahim, Gilerson et al. 2012). For example, Chami and Platel (2007) studied the use of directional variations and polarization of marine reflectance in the remote sensing retrieval of IOPs. Using an artificial neural network (NN), they demonstrated that adding polarized reflectance to unpolarized reflectance at 490 and 665 nm as inputs to the NN improves the retrieval of the scattering coefficient by more than 75% in relative error compared to the use of scalar reflectance alone. The remote sensing reflectance R_{rs} is defined as the water-leaving radiance normalized by the sum of direct and diffuse downwelling irradiances. To a first approximation, R_{rs} is proportional to b_b/a for open ocean waters and to $b_b/(a+b_b)$ for coastal waters, where b_b is the backscattering coefficient. As such, R_{rs} by itself does not contain any information on the light scattered forwardly into the water (Gordon, Brown et al. 1975, Gordon, Morel et al. 1983, Gordon, Brown et al. 1988, Gordon 1989). The extraction of coefficient b from coefficient c retrieved from polarization data can provide this information and reduce the retrieval uncertainty of b_b and a from R_{rs} data, especially in optically complex waters.

Studies have shown that the particulate attenuation coefficient, c_p, of hydrosols co-varies with the particulate organic carbon concentration (POC) as well as with phytoplankton carbon biomass (Behrenfeld and Boss 2003, Behrenfeld, Boss et al. 2005, Cetinic, Perry et al. 2012, Graff, Westberry et al. 2015). They suggest that there is a first-order relationship between the ratio of c_p to chlorophyll concentration (c_p:Chl), as an index of phytoplankton carbon (C) biomass ratio to chlorophyll concentration (C:Chl) and phytoplankton physiology, which is important for estimating primary production of the oceans. Thus, retrieval of the attenuation coefficient from remote sensing would allow for better understanding of the carbon cycle on the global scale, a primary goal of many ocean color satellite missions (e.g., PACE mission).

In coastal waters, hydrosols are composed primarily of two types of particles: algal and non-algal. Algal particles with high water content have a low refractive index (approximately 1.06) relative to that of water and therefore produce only an indistinctive polarization signature similar to that of Rayleigh scattering (Voss and Fry 1984, Tonizzo, Zhou et al. 2009). Their impact on the fraction of polarized light is predominantly by means of their absorption, which reduces the amount of multiple scattered light. Non-algal particles (NAP), such as mineral particles, scatter light more effectively due to their high relative refractive index, typically around 1.18 (Babin, Morel et al. 2003). Through multiple scattering, these particles can significantly decrease the polarization of water-leaving radiance; thus, their concentration should be retrievable using polarization measurements. Although this polarization is highly sensitive to underwater light scattering (Tonizzo, Gilerson et al. 2011), absorbing properties of the water also significantly impact the polarized light field, since the increase in absorption also results in the decrease of the number of the multiple scattering events; in turn this leads to an increase of the fraction of light that is polarized, and therefore, the increase of water absorption in the red part of the spectrum increases the fraction of polarized light. Similarly, the presence of colored dissolved organic matter (CDOM), a strong absorber of blue light, increases the fraction of polarized light in the blue part of the underwater spectrum (Chowdhary, Cairns et al. 2012).

In the open ocean, the majority of particles are algae and their by-products whose concentrations co-vary with chlorophyll *a* concentration [Chl]. These types of particles exhibit polarization patterns similar to those of molecular scattering because of their low refractive index (Chami, Santer et al. 2001). Underwater polarization for open oceans is therefore relatively simple (Voss and Fry 1984, You, Tonizzo et al. 2011). It can be reproduced well by vector radiative transfer

(RT) computations and persists in the water leaving radiance even when the sea surface is ruffled by strong winds (You, Kattawar et al. 2011, You, Tonizzo et al. 2011).

The advantage of using polarization measurements for remote sensing of oceans over scalar R_{rs} measurements is that the polarized components of light intrinsically (mathematically) carry more information about the microphysical properties of scattering particles. R_{rs} is dependent on only one element of the scattering matrix (*i.e.* scattering function) of hydrosols which is an IOP, and the absorption, while the polarized components are affected by all of the elements of the scattering matrix. Therefore, scattering and absorbing hydrosols modulate the polarization of light induced by molecular scattering of water molecules. Changes of light polarization depend on the concentration and composition of these hydrosols and thus can be related to both their absorption and scattering properties.

Timofeyeva (1970) found a relationship between the linearly polarized light in artificial milky turbid water and the parameter T, which is equal to the ratio of the attenuation coefficient of the scattered light flux to the direct light flux (Timofeyeva 1970). Inspired by this preliminary relationship, the work presented here seeks to expand that early study and extends it to naturally complex water conditions under natural illumination. It also expands the similar analysis of Ibrahim *et al.* (2012) (Ibrahim, Gilerson et al. 2012) to include a more realistic vector radiative transfer model in order to retrieve the attenuation coefficient, c, and the microphysical properties of hydrosols in the water body. The improvements in the model are focused on the development of a *hybrid* model that relates the microphysics to the macrophysics of hydrosol particles.

2. Background

2.1. Stokes parameters

A full description of light takes the electromagnetic (EM) vector nature of light into account and includes the intensity and the polarization state. The intensity is the energy flux of an EM wave (i.e., the brightness of light), and the polarization state fully describes an oscillating EM wave. In turn, a polarized beam of light can be defined by the 4×1 Stokes vector $\mathbf{I} = \{I, Q, U, V\}'$ (Mishchenko). Stokes parameter I is the intensity or radiance, which has the dimension of energy flux per unit solid angle (*i.e.* the total energy carried by the EM wave). Stokes parameters Q, U, and V describe the polarization state of the EM wave. The V component, which describes the amount of circular polarization, for most cases of light scattered in AO systems is negligible (Mishchenko). Therefore, one can confine the description of light scattered in AO systems to the intensity and linear polarization of an EM wave, which are given by the first three elements of the Stokes vector. A convenient measure for such cases is the degree of linear polarization (DoLP), which is defined as:

$$\mathrm{DoLP} = \frac{\sqrt{Q^2+U^2}}{I} \quad (1)$$

The DoLP describes the fraction of light, which is linearly polarized, so $0 \le \mathrm{DoLP} \le 1$. When DoLP = 1, it corresponds to a fully linearly polarized light, and DoLP = 0 corresponds to completely unpolarized light. All other values of DoLP indicate that the light is only partially linearly polarized.

2.2. Single scattering matrix

In scattering simulations of polarized light, it is important to define the scattering matrix **F**. This matrix relates the Stokes vector of light scattered by a particle to the Stokes vector of the incident light, and is therefore a 4×4 matrix, such that

$$\mathbf{I}_{sca}(\theta) = \mathbf{F}(\theta) \times \mathbf{I}_{inc}(\theta) \tag{2}$$

where θ is the scattering angle between the incident and scattered light. **I** is the Stokes vector of a light beam with the subscripts "sca", and "inc" corresponding to the scattered and incident beam, respectively. For scattering by homogenous spherical particles, **F** takes the form of (Kattawar, Hitzfeld.Sj et al. 1973, Hulst 1981):

$$\mathbf{F}(\theta) = \begin{bmatrix} F_{11} & F_{12} & \mathbf{0} & \mathbf{0} \\ F_{12} & F_{11} & \mathbf{0} & \mathbf{0} \\ \mathbf{0} & \mathbf{0} & F_{33} & F_{34} \\ \mathbf{0} & \mathbf{0} & -F_{34} & F_{33} \end{bmatrix}, \tag{3}$$

The (1,1) element of the scattering matrix **F**, F_{11}, is the scattering function. The scattering matrix is calculated from the particle refractive index and the particle size distribution (PSD) of a group of particles using the Mie theory detailed in Section 3.2.1.

2.3. Multiple scattering in the AO System

The following assumptions are made for the AO system: (1) the medium is plane parallel, and (2) only vertical variations of the medium are considered. The RayXP program, developed by Zege *et al.*, is used to calculate the Stokes vector of the light scattered within the AO system (Zege, Katsev et al. 1993, Tynes, Kattawar et al. 2001). The RayXP program performs accurate and extremely fast computations by simulating the Stokes vector of light within any stratified system, achieved by coupling of two methods: (1) the adding-doubling method and (2) the Multi-component approach (MCA). The MCA dramatically reduces the computational time for the cases that involve strong anisotropy in scattering by separating the scattering matrix of the scatterers into two main components. It separates the peaked component from the more diffused remaining component of the scattering matrix. Each of these two separate components is further divided into multiple components that are generally easy to solve for multiple scattering computations.

3. Study cases

3.1. Atmosphere

The atmosphere is assumed to consist of two homogeneous layers. The top layer is a molecular (Rayleigh scattering) layer. The optical thickness values for this layer are taken from MODIS products to be 0.098 at 550 nm (Ahmad, Franz et al. 2010). The molecular optical properties are obtained from the standard data bank provided by RayXP, and give a molecular depolarization factor of 0.0279 (Hansen and Travis 1974, Young 1980). The bottom layer is assumed to be a continental aerosol layer with optical thickness τ of 0.1 at 400 nm The continental aerosol model is obtained from a data bank based on simple aerosol models from well-known climatological atmosphere models, which assume a composition made up of 70% dust, 29% water soluble, and 1% carbon soot aerosols.

3.2. Ocean

The ocean body is assumed to consist of a single *(i.e.* homogeneous) layer with infinite depth. The benthic optical effects at the bottom of the ocean are not taken into consideration. For the interface between the ocean and the atmosphere (*i.e.* water surface) we use the isotropic distribution of surface slopes given by Cox and Munk (Cox and Munk 1956) for a wind speed of 3 m/s. The computation of micro-physical optical properties for the ocean body is discussed in the next section. The macroscopic optical properties for the ocean body are discussed in Section 3.2.2.

3.2.1. Microphysical optical properties (Scattering Matrices)

To obtain the scattering matrices as an input for the radiative transfer (RT) program RayXP, Mie calculations were used for both phytoplankton and non-algal particles (NAP) in oceanic bodies. The input parameters for these calculations are the real part of the particle refractive index and the PSD. Open ocean (Case I) waters are assumed to contain only phytoplankton particulate, whereas coastal ocean (Case II) waters are assumed to contain both phytoplankton and NAP particulate. For simplification, it is also assumed that both types of particles are homogeneous spheres with particle radii between 0.1 and 50 μm that follow a Junge-type PSD. The Junge slope parameters ξ_{ph} and ξ_{nap} for the phytoplankton and NAP matter PSD, respectively, vary each between 3.5 and 4.5. The phytoplankton refractive index n_{ph} is fixed at 1.06 (relative to water), whereas the NAP refractive index n_{nap} is allowed to vary from 1.15 to 1.21 (relative to water). The corresponding phytoplankton and NAP scattering matrices are calculated using the Mie code described by Mishchenko *et al*. (Mishchenko, Travis et al. 2002)

The RayXP program requires as input the bulk ocean scattering matrix, which consists of a weighted average of the plankton and NAP scattering matrices. For the weights, we use the phytoplankton and NAP scattering coefficients *b* from Ibrahim *et al.* 2012 (Ibrahim, Gilerson et al. 2012).

3.2.2. Macrophysical optical properties (bulk absorption and scattering coefficients)

The macrophysical optical modeling of bulk oceanic waters is divided into two distinctive cases: open ocean (Case I) and coastal ocean (Case II). Case I oceans contain mainly phytoplankton particles and other co-related, co-variant products such as Color Dissolved Organic Matter

(CDOM). Case II waters are impacted by strong interactions with rivers, shores, and anthropogenic activities which make them optically complex because they contain substantial amounts of sediments and minerals whose variability does not depend on the amount of phytoplankton. In what follows, we use chlorophyll *a* concentration [Chl] as a proxy for the amount of phytoplankton. It should be noted that coastal regions can contain high concentrations of phytoplankton (algal blooms), and such eutrophic regions are not considered in this study. The next subsections explain the modeling of the optical properties for Case I and Case II waters separately.

A. Case I waters

For Case I waters, a three-component model is assumed: seawater, phytoplankton particles, and CDOM. The presence of NAP matter is ignored for these waters. The scattering and absorption coefficients b_w and a_w of seawater are taken from Morel 1974 and Pope and Fry (1997), respectively (Morel 1974, Pope and Fry 1997). Since the water molecules and density fluctuations are much smaller in size than the visible wavelength, their scattering matrix can be obtained from the Rayleigh scattering theory. Inelastic scattering, such as Raman scattering, is not taken into consideration in our RT simulations.

Following the empirical relationship detailed in Bricaud *et al*. (1998) (Bricaud, Morel et al. 1998), the absorption coefficient of phytoplankton, $a_{\mathrm{ph}}(\lambda)$, is calculated from the empirical coefficients $A(\lambda)$ and $E(\lambda)$. The phytoplankton scattering coefficient $b_{ph}(\lambda)$ is calculated as the difference between the phytoplankton spectral attenuation coefficient $c_{ph}(\lambda)$ and absorption coefficient $a_{\mathrm{ph}}(\lambda)$. The attenuation coefficient at 550 nm, $c(550)$, is obtained from the sum of the absorption coefficient $a_{ph}(550)$ and scattering coefficient $b_{ph}(550)$ at 550 nm, which is obtained from Morel and Maritorena (2001) (Morel and Maritorena 2001). The spectral behavior of $c_{ph}(\lambda)$ is modeled using the power law function given by the Hydrolight RT program (Morel, Antoine et al. 2002, Mobley and Sundman 2008).

The absorption coefficient $a_g(\lambda)$ of CDOM decreases exponentially with increasing wavelength. CDOM is a poor scatterer of light and its scattering properties can be neglected for the visible spectrum (Carder, Chen et al. 1999, Babin, Stramski et al. 2003, IOCCG 2006). The absorption coefficient of CDOM at 400 nm, $a_g(400)$ is correlated randomly within 20% (+/- 10%) to the phytoplankton and water absorption coefficients at 400 nm as well. Figure 1 shows the block diagram of the RT modeling for Case I waters.

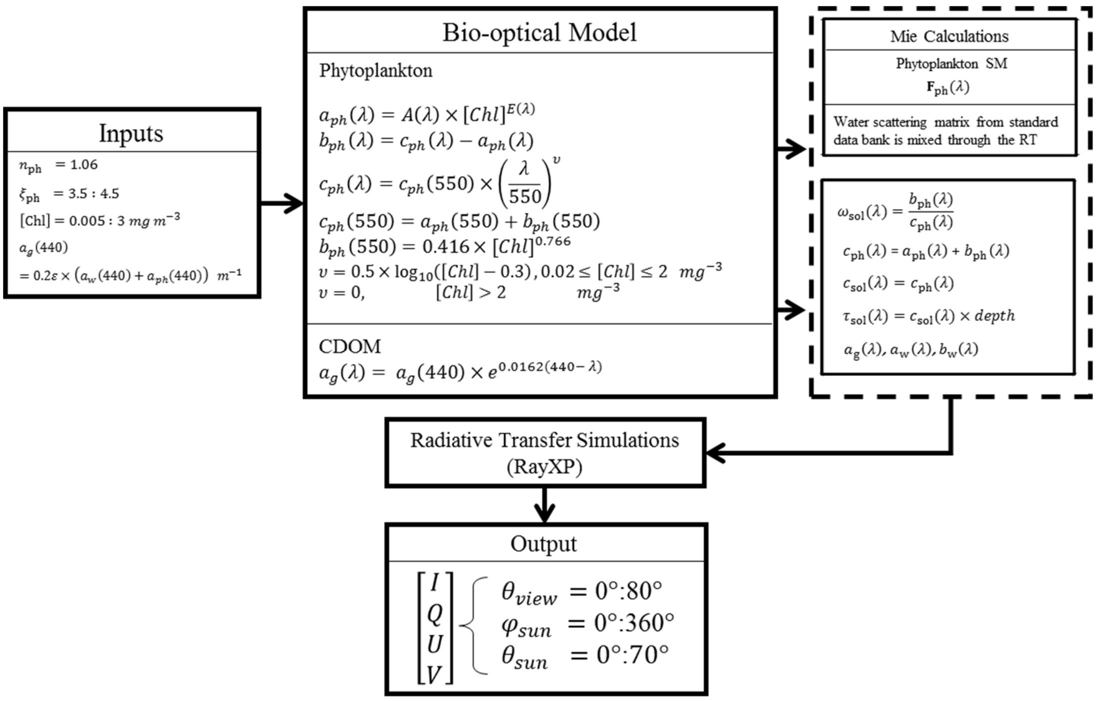

Figure 1. Flow Diagram of the bio-optical and RT models for the generation of the data set for Case I waters.

B. Case II waters

For Case II waters, a four-component model is assumed that includes seawater, phytoplankton particles, CDOM, and NAP matter. The specific absorption coefficient of phytoplankton particles $a^*_{ph}(\lambda)$ is modeled as the combination of specific absorption by two dominant phytoplankton species (*i.e.,* micro- and pico-plankton particles), weighted by their size parameter S_f (Ciotti, Lewis et al. 2002). The total phytoplankton absorption coefficient $a_{\mathrm{ph}}(\lambda)$ is then calculated as the product of $a^*_{ph}(\lambda)$ and $[Chl]$. The scattering coefficient of phytoplankton $b_{\mathrm{ph}}(\lambda)$ is obtained as the difference between the phytoplankton attenuation c_{ph} and absorption $a_{\mathrm{ph}}(\lambda)$ coefficients (Stramski, Bricaud et al. 2001, IOCCG 2006). The spectral behavior of $c_{\mathrm{ph}}(\lambda)$ is modeled as a power law function with spectral slope Y_{ph} (IOCCG 2006). Note that Y_{ph} is directly related to the slope ξ_{ph} for the Junge PSD of phytoplankton particles, such that $Y_{\mathrm{ph}} = \xi_{\mathrm{ph}} - 3$ (Twardowski, Boss et al. 2001). The phytoplankton attenuation coefficient at 550 nm, $c_{ph}(550)$, is calculated following Gilerson *et al.*, 2007 (Gilerson, Zhou et al. 2007).

The absorption spectrum of NAP is modeled as a decaying exponential function following Babin *et al.* (2003) (Babin, Stramski et al. 2003). On the other hand, the scattering coefficient is based on the microphysical properties of NAP matter. This coefficient is modeled as the product of the specific scattering coefficient $b^*_{nap}(\lambda)$ and the concentration of NAP matter $[NAP]$, where $b^*_{nap}(\lambda)$ is calculated as follows (Wozniak and Stramski 2004):

$$b^*_{nap}(\lambda) = \frac{3\bar{Q}_b(\lambda)}{2\rho}\frac{\int_{D_{min}}^{D_{max}} N(D)D^2 dD}{\int_{D_{min}}^{D_{max}} N(D)D^3 dD}, \qquad [m^2\ g^{-1}] \qquad (4)$$

In Eq. (4), $\bar{Q}_b(\lambda)$ is the average spectral efficiency factor, ρ is the particle density, D is the particle diameter, and $N(D)\mathrm{d}D$ is the particle size distribution. Following Sec. 3.2.1 we adopt the Junge PSD with Junge slope parameter $3.5 \leq \xi_{\mathrm{nap}} \leq 4.5$ for $N(D)\mathrm{d}D$, and the refractive index $1.15 \leq n_{\mathrm{nap}} \leq 1.22$, as input for Mie computations to obtain $\bar{Q}_b(\lambda)$. The density ρ of NAP matter is dependent on the composition of this matter. Assuming an ensemble of 29 mineral species, this density is calculated as follows (Wozniak and Stramski 2004)

$$\rho = 6.779 \times 10^{6} \times n_{nap} + 5.232 \times 10^{6} \qquad [g\ m^{3}] \qquad (5)$$

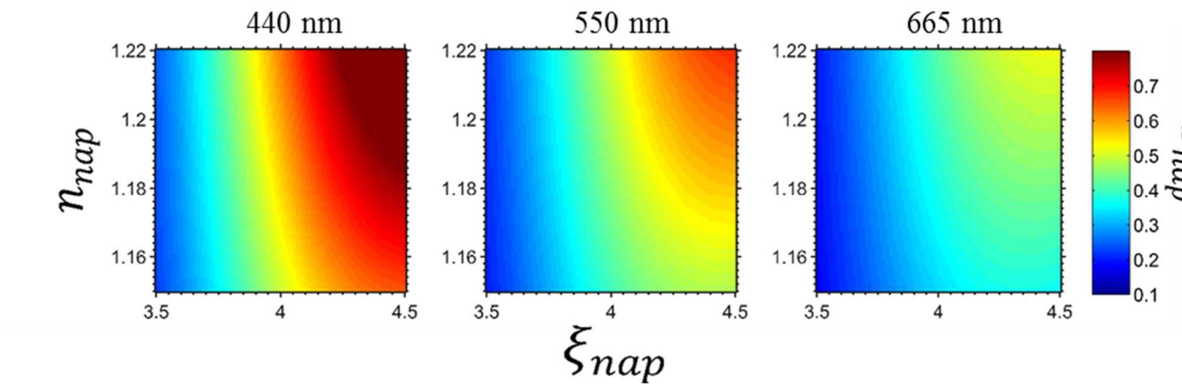

Figure 2. The specific scattering coefficients b^*_{nap} of NAP according to the Mie theory for 440 nm, 550 nm, and 665 nm.

Figure 2 shows the relationship among ξ_{nap}, n_{nap}, and b^*_{nap}. The refractive index n_{nap} is assumed to be in the range 1.15-1.22 relative to the water, while the values of the Junge slope ξ_{nap} range from 3.5 to 4.5, which is typical for NAP particles. It is considered a more realistic approach to have b^*_{nap} vary with ξ_{nap} and with n_{nap}. In our previous study (Ibrahim, Gilerson et al. 2012), as a first approximation, b^*_{nap} was assumed to be constant over the wavelength and for different PSD, which is not accurate as shown in Figure 2 . It is important to note that the variation of b^*_{nap} with n_{nap} is weaker than the variation of b^*_{nap} with ξ_{nap} and Y_{nap}, which validates a part of our previous study. The slope of the NAP spectral scattering coefficient, Y_{nap}, is defined as $\xi_{nap} - 3$.

The spectral scattering coefficient $b_{nap}(\lambda)$ calculated from Mie theory can have values 5-30% higher in the blue part of the spectrum when the imaginary part of the refractive index is set to zero in these computations (*i.e.* assuming $a_{nap}(\lambda)$ is zero) (Doxaran, Ruddick et al. 2009). In order to correct for the resulting change in $b_{nap}(\lambda)$ spectra, an empirical model based on theoretical calculations is used to reproduce the actual spectra of $b_{nap}(\lambda)$ from the red channel (665 nm) to the blue channels for non-zero $a_{nap}(\lambda)$ values. This model is given by Doxaran et al. (Doxaran, Ruddick et al. 2009)

$$b_{nap}(\lambda) = b_{nap}(665) \times \left(\frac{\lambda}{665}\right)^{-Y_{nap}} - \left(1 - \tanh\left[0.5 \times Y_{nap}^2\right]\right) \times a_{nap}(\lambda) \quad [m^{-1}]$$

(6)

The block diagram in Figure 3 shows the flow diagram of our RT computations for Case II waters.

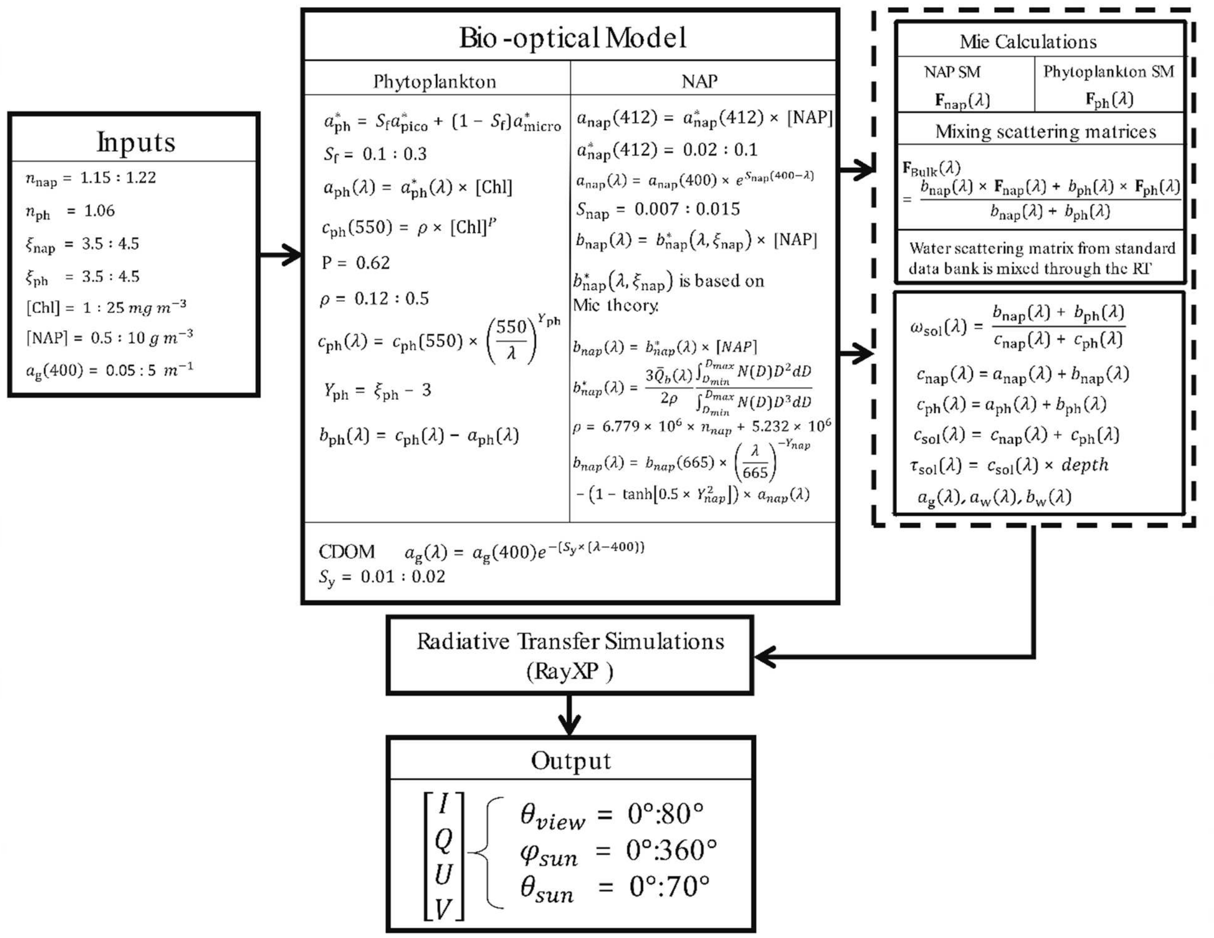

Figure 3. Flow Diagram of the bio-optical and RT models for the generation of the data set for Case II waters.

4. Results of radiative transfer simulations

Simulated RT values of DoLP are investigated to seek a definitive empirical relationship with the IOP ratio *c/a* at three wavelengths: 440, 550, and 665 nm. Such a relationship would provide the possibility of retrieving the attenuation coefficient, *c*, of the water constituents from data obtained by under- or above-water polarization radiometric measurements of upwelling radiation, since the absorption coefficient, *a*, is routinely estimated from the remote sensing reflectance using well-established algorithms (Lee, Carder et al. 2002).

4.1. Geometrical interpretation of the RT results

The RT program, RayXP, provides the Stokes parameters as a function of the viewing and azimuth angles. The Sun zenith angle is varied from 0° zenith when the Sun is overhead to 70° when the Sun is near the horizon. The 0° azimuth angle corresponds to the condition when the Sun and the viewer are in opposition, while 180° azimuth angle corresponds to the condition when the Sun is behind the sensor (*i.e.* the sensor and the Sun are in the same half plane). The geometry of the incident, viewing, and azimuth angles is shown in Figure 4.

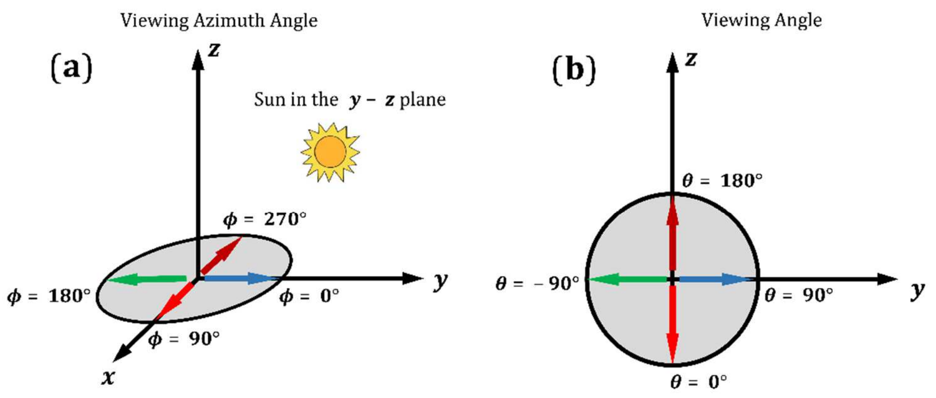

Figure 4. Geometrical interpretation of: (a) the viewing azimuth angle and (b) the viewing angle for RayXP simulations. Arrows point into viewing direction

We also define the scattering angle, θ_{sca}, as the angle between the incident light and the scattered light (*i.e.* the viewing direction). Based on Ibrahim *et al.* (2012) (Ibrahim, Gilerson et al. 2012), the best viewing geometries for above water polarization measurements call for a viewing angle between 40° and 60° from the nadir direction, and a relative azimuth of 90° with respect to the Sun to avoid Sun glint. Therefore, the results presented here will be at 40° viewing angle and with two relative azimuth angles of 0° and 90° with respect to the plane containing the Sun.

4.2. Case I simulation results

The RayXP results presented in this section show the variability of the $DoLP^{0-}$ at just below the air-water interface as a function of the ratio between the attenuation and the absorption coefficients at 440, 550, and 665 nm. DoLP in-water is mainly affected by the scattering process of the particulates, which consist only of phytoplankton as assumed in our bio-optical model (Figure 1). The absorption of light modulates the changes in the DoLP by reducing the number of scattering events in the water or by reducing the single scattering albedo.

Based on the bio-optical model, the largest variability in *c/a* occurs at 550 nm and 440 nm and smallest at 665 nm, due to the constant high seawater absorption as compared to the absorption and attenuation particulate and dissolved components. That in turn drives the dynamic range of the resultant $DoLP^{0-}$, spectrally. Figure 5 shows the relationship between the $DoLP^{0-}$ and *c/a* for 40° viewing zenith angles and for azimuth viewing angles of 0° and 90° respectively.

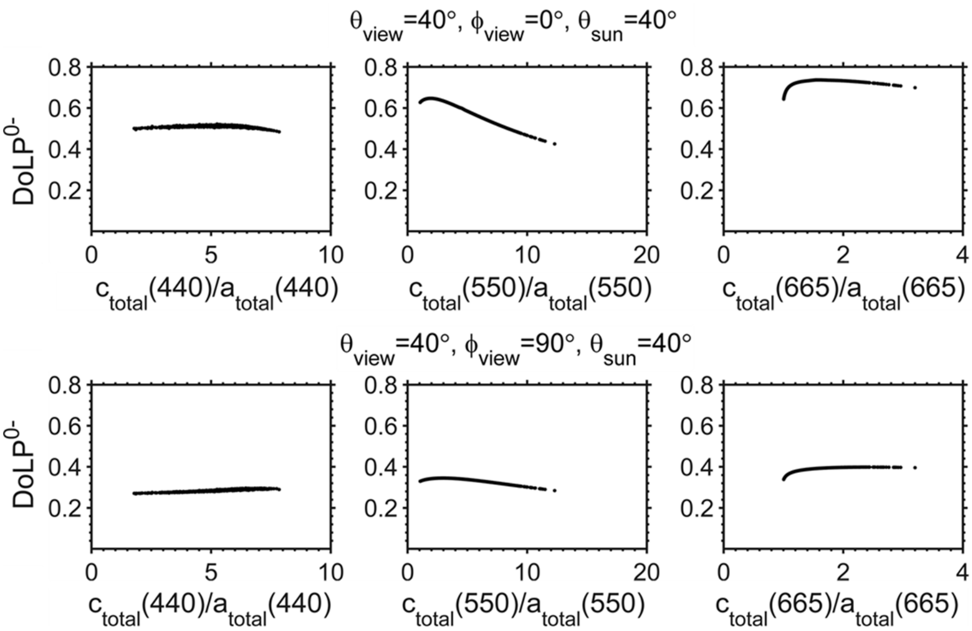

Figure 5. Relationship between $DoLP^{0-}$ just below the sea surface at θ_{view} = 40° and φ_{view} = 0° (θ_{sca} = 111.2°) and 90° (θ_{sca} = 132.2°) and c/a ratio at three wavelengths.

The variability of the $DoLP^{0-}$ as a function of the *c/a* ratio is minimal for the 440 and 665 nm for the 0° azimuth viewing angle. At 550 nm, a noticeable variation exists in the relationship for most of the viewing geometries since the phytoplankton particles are the dominant constituent in these water, the $DoLP^{0-}$ becomes sensitive to their scattering coefficient in the green wavelength channel, where the DoLP is not dominated by Rayleigh scattering (as in the blue channel) and by the high water absorption (as in the red channel). Therefore, the variability of the *c/a* ratio due to the variations at 550 nm is high as compared to the blue and red channels.

The changes of the $DoLP^{0-}$ versus *c/a* ratio at 90° relative azimuth angle are small. That could be due to the value of the scattering angle for this geometry (scattering angle is about 132°) which is higher than that corresponding to the geometry of 0° relative azimuth (scattering angle is about 111°). DoLP is less sensitive to the composition of hydrosols at 132° than at 111° scattering anlge. Despite the 90° relative azimuth angle is a preferred geometry for above water detection of the polarized water leaving radiance, the invariance of the signal versus the *c/a* ratio and therefore the [Chl] does not allow retrieval. These results corroborate with those of Harmel *et al.* (Harmel and Chami 2008, Harmel and Chami 2012).

To understand the geometrical constraints on the variability of $DoLP^{0-}$ versus c/a, we examine in Figure 6 the Dynamic Range (DR) of DoLP that is defined as follows

$$DR(\theta_{view}, \varphi_{view}) = \frac{DoLP^{0-}(\theta_{view}, \varphi_{view})_{max} - DoLP^{0-}(\theta_{view}, \varphi_{view})_{min}}{DoLP^{0-}(\theta_{view}, \varphi_{view})_{theoritical\_max} - DoLP^{0-}(\theta_{view}, \varphi_{view})_{theoritical\_min}}, \quad (7)$$

The DR is calculated for each viewing and azimuth angle as the difference between maximal and minimal $DoLP^{0-}$ for the same geometry normalized by the difference between theoretical maximal and minimal $DoLP^{0-}$ simulated for all cases of IOPs at each specific geometry. The theoretical maximum is calculated from pure water (Rayleigh scattering) conditions, while theoretical minimum is zero. The DR values vary between 0% and 50% of the maximal possible $DoLP^{0-}$ simulated with RayXP at each geometry. Higher DR values explain a large variability in the relationship and therefore allow for retrievals at specific viewing geometries.

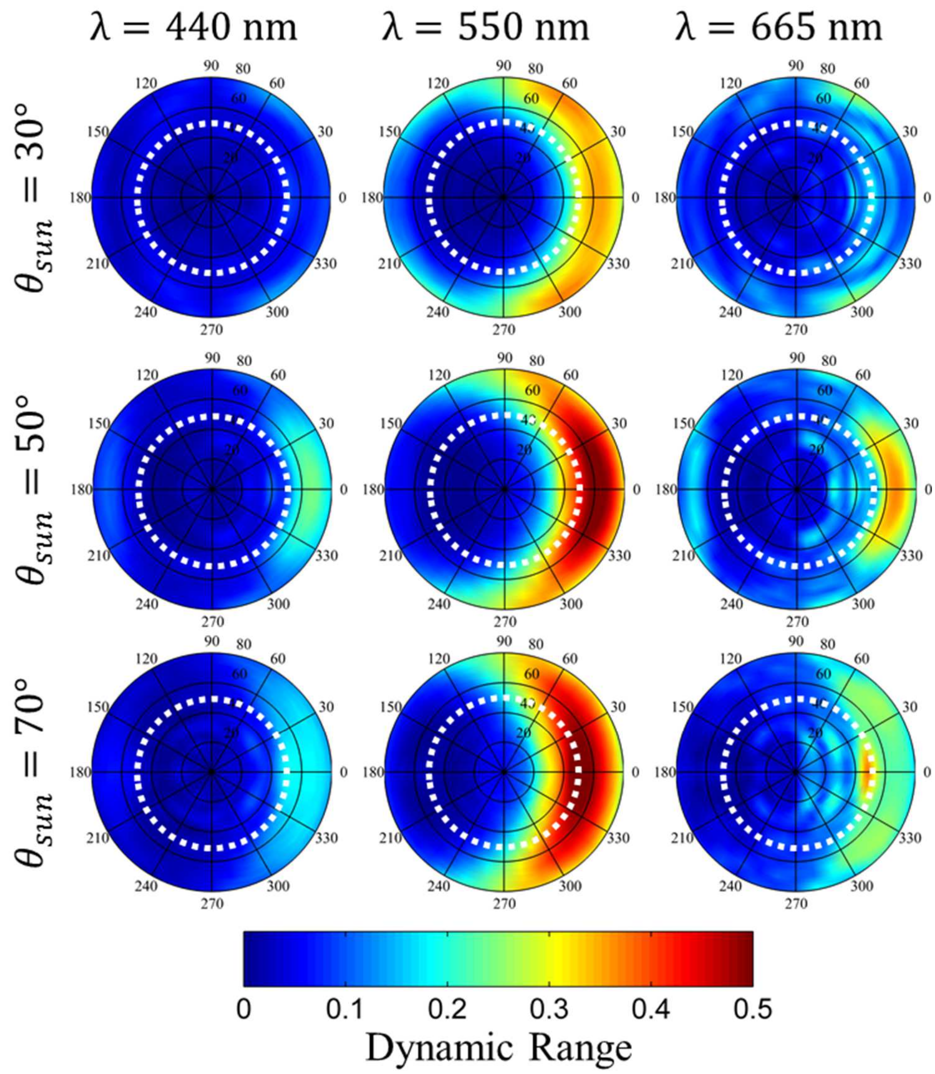

Figure 6. Synoptic view of the Dynamic Range (DR) at just below the air-water interface for Sun relative azimuth from 0° to 360° (0° azimuth is for Sun and sensor are in opposition) and viewing angle of upwelling polarized light from 0° to 80° (0° viewing angle is for sensor looking vertically downward) for three Sun zenith angles 30°, 50°, and 70° and for three wavelength 440, 550, and 665 nm. Dashed white circles represent the border of Snell's window.

Figure 6 shows the DR for all viewing geometries of the upwelling light at just below the air-water interface at three Sun zenith angles and at three wavelengths (440, 550, and 665 nm). Lower values of DR show invariability of the $DoLP^{0-}$ versus c/a ratio, thus making retrievals not possible due to the lack of sensitivity in the relationship; on the other hand, higher DR shows more variability in the $DoLP^{0-}$ versus c/a for which retrieval is possible. Figure 6 demonstrates that the DR is low at 440 and 665 nm for all of the geometries that corroborates with the scatter plots shown in Figure 5. At 550 nm, the DR exhibits high values mainly in the principal plane of the Sun (*i.e.* $\varphi_{view} = 0°$) and near it. DR values in that scenario can approach 50% of the theoretical DR assumed, showing the high sensitivity of $DoLP^{0-}$ to variations in c/a at 550 nm allowing retrievals. It is important to note that such a relationship depends highly on the Sun zenith angle. Lower Sun angles (*i.e.,* larger zenith angle) show an increase in the DR as opposed to a near overhead Sun. This analysis is done for underwater polarization, $DoLP^{0-}$ and therefore, measurements of the polarized water-leaving radiance, and will be affected by ocean surface transmission, which limits $\theta_{view} \leq 48°$. Furthermore, the Sun and sky glint corrections will make retrievals even more challenging from above-water measurements. Nevertheless, several options of above-water polarimetric observations in Case I waters should be further studied, including possibilities of measurements in or near the principal plane ($0° \leq \varphi_{view} \leq 60°$) but with different Sun and viewing angles to minimize Sun glint effects. Also of interest for future studies are considerations of more complex (but closer to real) configurations of the phytoplankton particles, with a broader range of refractive indices and hyperspectral measurements of the DoLP or even Stokes components Q/I and U/I, which can reveal more features in polarization signatures and facilitate additional relationships and retrievals.

4.3. Case II simulation results

4.3.1. Assessment of the relationship between DoLP and *c/a* below the water

Results for Case II water simulations at depths just below the air-water interface are presented next at three wavelengths: 440, 550, and 665 nm. Figure 7 shows the variability of the $DoLP^{0-}$ versus *c/a* ratio at 40° viewing angle and azimuth angles 0° and 90°. For this figure, we fix a single solar zenith angle at 40° and vary the viewing angle to cover the largest range of scattering angles in the backward direction. There is a strong relationship between the $DoLP^{0-}$ values and *c/a* ratios with high variability in the broad range of both parameters for these specific viewing angles in the Sun's principal plane, and at 90° away from it. As a result, it is possible to easily fit the relationship, which allows us to retrieve the attenuation coefficient from the DoLP measurements if the absorption coefficient *a* is known (note, *a* can be retrieved with reasonable accuracy using inversion algorithms with good atmospheric correction (AC), although AC can be challenging over turbid waters (Lee, Carder et al. 2002, Ahmad, Franz et al. 2010, Goyens, Jamet et al. 2013)).

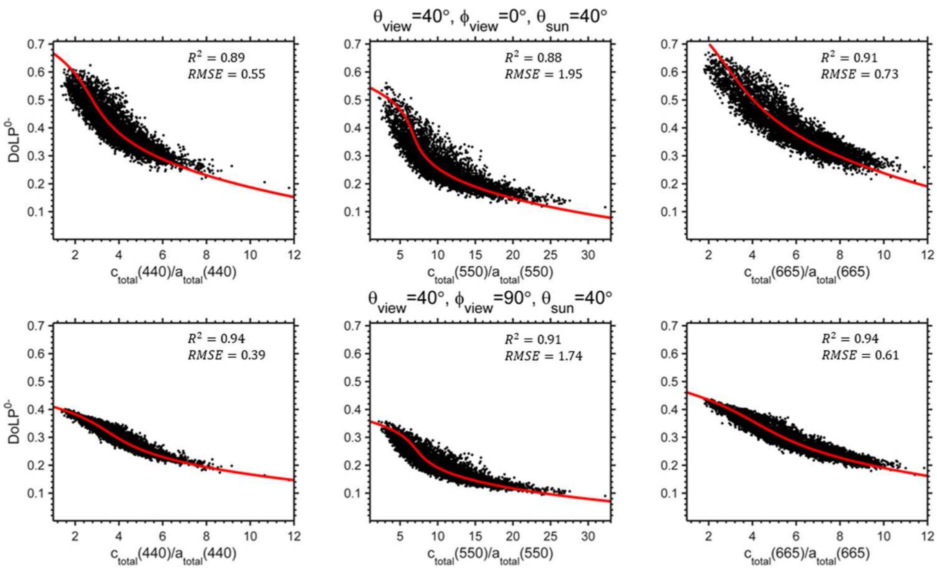

Figure 7. Fitted relationship between DoLP^{0-} just below the sea surface at θ_{view} = 40° and φ_{view} = 0° ($\boldsymbol{\theta_{sca}}$ = 111.2°) (first row) and 90° ($\boldsymbol{\theta_{sca}}$ = 132.2°) (second row) and c/a ratio at three wavelengths.

The red lines in Figure 7 are parameterizations obtained by fitting a third-order polynomial as follows:

$$\left(\frac{c}{a}\right)_{fit} = p_3 \times (DoLP)^3 + p_2 \times (DoLP)^2 + p_1 \times (DoLP)^1 + p_0 \qquad (8)$$

Here, a and c are the absorption and attenuation coefficients, respectively; p_0 to p_3 are the polynomial fitting coefficients which vary with the viewing zenith and azimuth angles $\boldsymbol{\theta_{view}}$ and $\boldsymbol{\varphi_{view}}$. Furthermore, DoLP ≡ DoLP^{0-} for Figure 7.

The quality of the fitting of Eq. 8 can be estimated by calculating the root mean squared error (RMSE) or the coefficient of determination R^2 coefficient defined as

$$R^2 = \frac{SSR}{SST} = \frac{\sum_{i=1}^{5000}\left[\left(\frac{c}{a}(DoLP_i)\right)_{fit} - \overline{\left(\frac{c}{a}\right)}_{fit}\right]^2}{\sum_{i=1}^{5000}\left[\left(\left(\frac{c}{a}\right)_i\right) - \overline{\left(\frac{c}{a}\right)}_{fit}\right]^2}, \qquad (9)$$

In Eq. 9, SSR is the sum of squared differences between the regression fit ($(c/a(DoLP_i)_{fit})$) and the sample mean $\overline{c/a}$, and 'i' iterates from 1 to 5000 different cases of IOPs in the RT simulations. SST stands for the sum of squares total, which means the sum of squared deviations of the (c/a) values around their mean. High values of R^2 indicate good fitting qualities and vice-versa.

The average error in the fitting, RMSE, is defined as

$$RMSE = \sqrt{\frac{\sum_{i=1}^{5000}\left[\left(\frac{c}{a}(DoLP_i)\right)_{fit} - \overline{\left(\frac{c}{a}\right)}_{fit}\right]^2}{5000}} \qquad (10)$$

In order to have a synoptic view of the fitting quality, the R^2 values are plotted in Figure 8 for all viewing geometries available for a given solar angle (*i.e.* θ_{sun} = 20° to 70°). From this figure, we can estimate the range of geometries that permit the best retrieval of c from measurements of the DoLP just below the ocean surface.

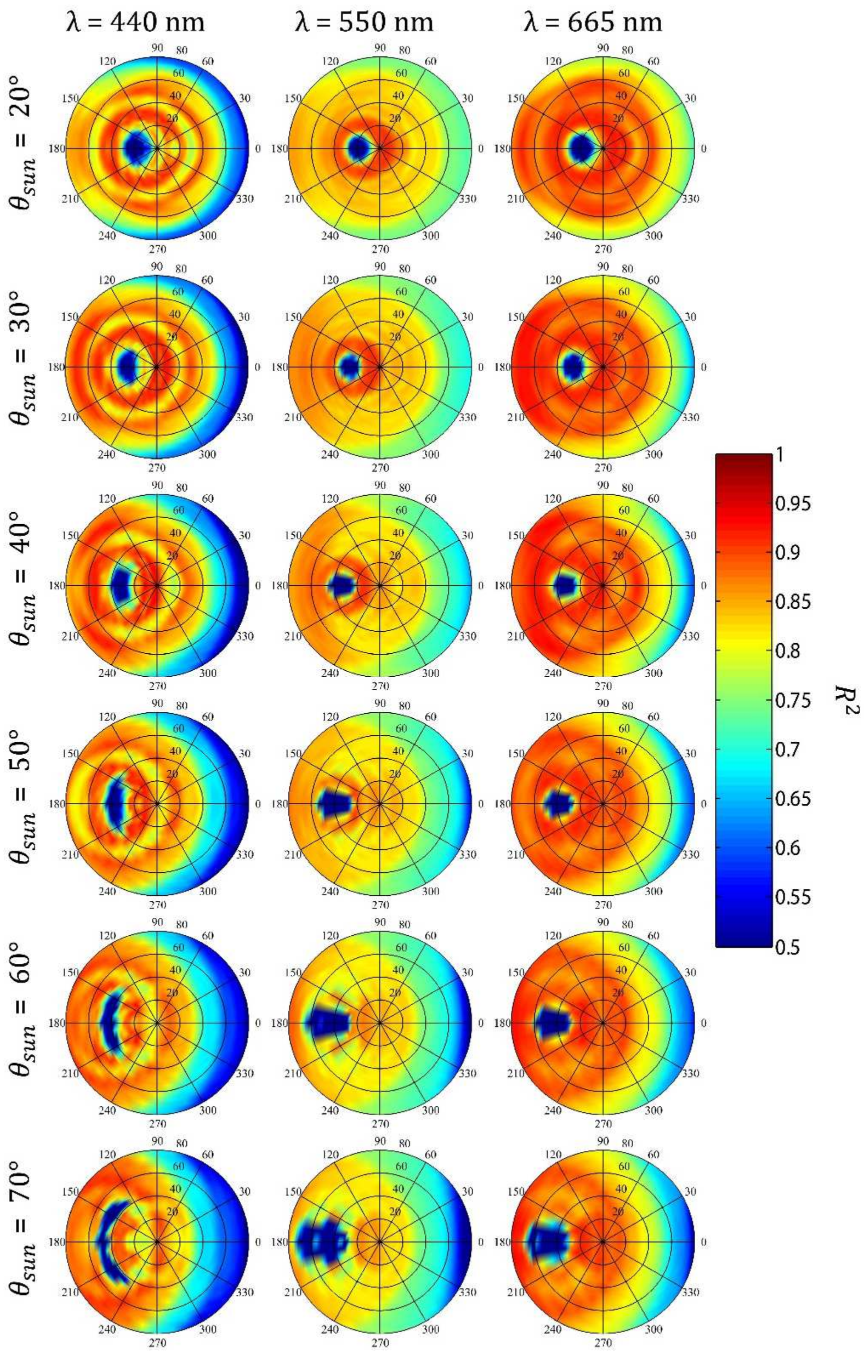

Figure 8. Synoptic view of the coefficient of determination R^2 at just below the air-water interface for Sun relative azimuth from 0° to 360° (0° azimuth is for Sun and sensor are in opposition) and viewing angle of upwelling polarized light from 0° to 80° (0° viewing angle is for sensor looking vertically downward).

In Figure 8, the coefficient of determination (R^2) is higher than 0.9 for 665 nm and higher than 0.8 for 440 and 550 nm for most of the viewing geometries below the water surface, which indicates a good and consistent relationship between the simulated data set and parameterization using Eq. 8. It is also noticeable that R^2 degrades in the backscattering direction where the DoLP is minimal. The high R^2 correlation for other viewing geometries in Figure 8 is very promising when considering future air- or space-borne measurements of the polarized water-leaving radiance, since it does not limit the range of viewing angles at which this type of sensor operates. For example, the good correlation that exists at the meridian plane away from the Sun's principal plane (e.g., 90° away and therefore away from Sun glint contaminations) makes the measurements of polarized water-leaving radiance easier and more accurate and creates the possibility of a direct estimation of the attenuation coefficient, which is otherwise physically impossible when using above-water sensors. As already mentioned above, this method to retrieve the attenuation coefficient of hydrosols can be used to study carbon-based ocean productivity and phytoplankton physiology from remote sensing (Behrenfeld, Boss et al. 2005, Cetinic, Perry et al. 2012). Figure 8 shows that excellent R^2 values can be achieved, especially at 440 and 665 nm, for a broad range of azimuth and viewing angles. This is most likely due to the moderate absorption (usually dominated by the water absorption at 665 nm and CDOM absorption at 440 nm), which reduces the number of the scattering events and increases the DoLP in comparison with 550 nm cases.

Table 1 below shows the polynomial fitting coefficients for $\theta_{view} = 40°$ and Sun relative azimuth angle $\phi_{view} = 90°$ at all three wavelengths for $\theta_{sun} = 30°$ and $\theta_{sun} = 50°$ respectively.

Table 1. Fitting coefficients of the polynomial function for $\theta_{view} = 40°$, $\phi_{view} = 90°$, and $\theta_{sun} = 30°$ (θ_{sca} = 135.3°) and $\theta_{sun} = 50°$ (θ_{sca} = 128.8°).

Fitting Coefficients	***Wavelength (nm)***					
	440		**550**		**665**	
	$\boldsymbol{\theta_{sun} = 30°}$	$\boldsymbol{\theta_{sun} = 50°}$	$\boldsymbol{\theta_{sun} = 30°}$	$\boldsymbol{\theta_{sun} = 50°}$	$\boldsymbol{\theta_{sun} = 30°}$	$\boldsymbol{\theta_{sun} = 50°}$
$\boldsymbol{P_3}$	-1540	-783	-4179	-2407	-734	-350
$\boldsymbol{P_2}$	1291	808	2907	2037	692	414
$\boldsymbol{P_1}$	-384	-296	-709	-602	-243	-184
$\boldsymbol{P_0}$	44	41	67	69	35	34

4.3.2. The retrieval of the concentration of minerals [NAP] from above water

The DoLP of upwelling light, either below or above the ocean surface, is highly sensitive to the scattering properties of high-refractive hydrosols. Our radiative transfer simulations show that there is a strong relationship between the scattering coefficient of high-refractive NAP matter and the DoLP. This relationship extends to the concentration [NAP] of high-refractive NAP matter such as minerals. Based on the conventional understanding of the polarization nature of light, higher scattering coefficients or high NAP concentrations lead to a higher number of multiple scattering events, therefore lowering the DoLP and vice versa. Such behavior is observed in Figure 9 for b_{nap} and in Figure 10 for [NAP]:

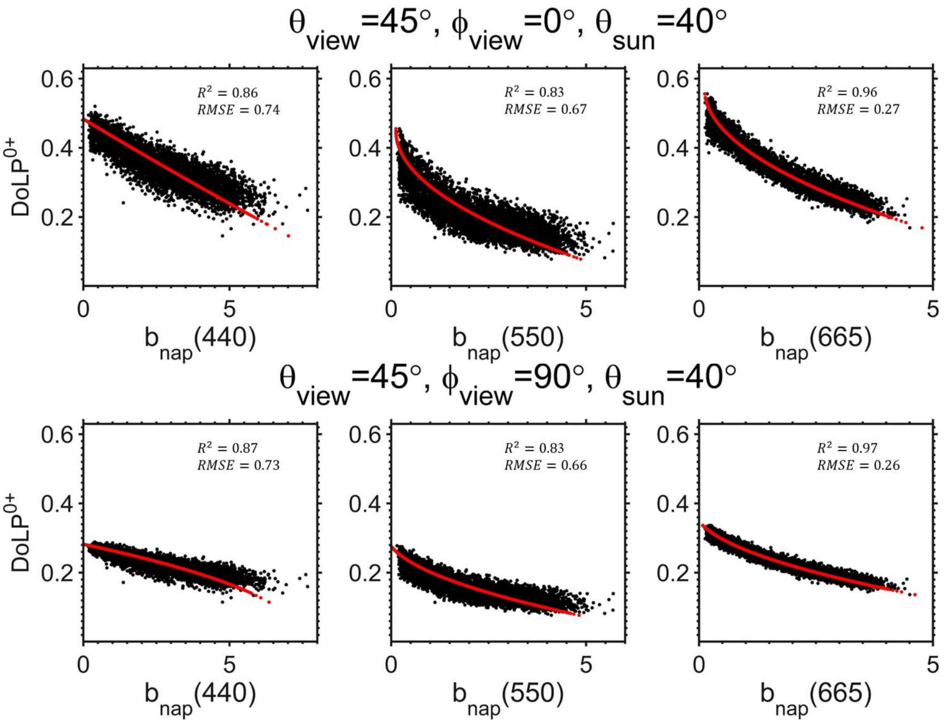

Figure 9. Fitted relationship between DoLP^{0+} just above the sea surface at θ_{view} = 45° and φ_{view} = 0° ($\boldsymbol{\theta_{sca}}$ = 95°) (first row) and 90° ($\boldsymbol{\theta_{sca}}$ = 122.8°) (second row) and $\boldsymbol{b_{nap}}$ at three wavelengths.

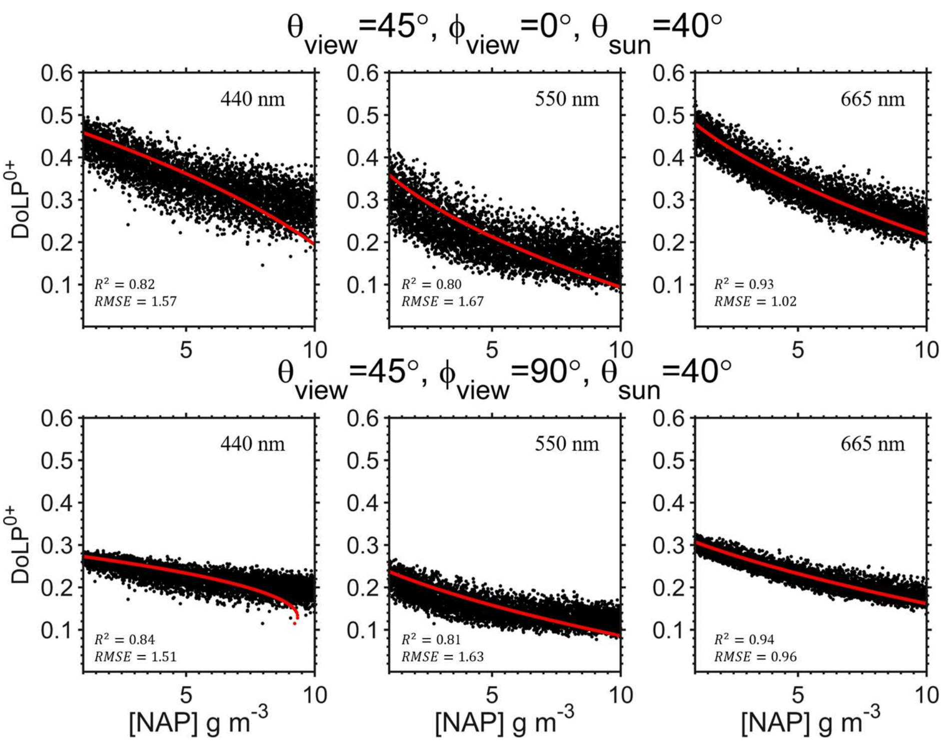

Figure 10. Fitted relationship between DoLP^{0+} just above the sea surface at θ_{view} = 45° and φ_{view} = 0° (θ_{sca} = 95°) (first row) and 90° (θ_{sca} = 122.8°) (second row) and NAP at three wavelengths.

The DoLP^{0+} above water surface was calculated from the Stokes vector below the surface using the transmission Mueller matrix for a flat sea-surface give by Kattawar and Adams (1989) (Kattawar and Adams 1989). The co-variation of DoLP^{0+} with b_{nap} and with [NAP] is clearly observed, especially at 665 nm, because the polarization of light is mainly driven by the dominant NAP scattering particles in coastal waters. The DoLP becomes less affected by other constituents such as phytoplankton and CDOM absorption or phytoplankton scattering at the red part of the spectrum. Such relationships can be effective in retrievals by themselves and in a combination with typical retrievals of [NAP] from remote sensing reflectance at 665 nm (Babin, Morel et al. 2003, Babin, Stramski et al. 2003).

4.3.3. The retrieval of the microphysical properties from above water

The microphysical properties of hydrosols include but are not limited to the refractive index and the size distribution. The polarization of scattered underwater light, and therefore of water-leaving radiance, is highly sensitive to these properties. One can retrieve such particulate properties from multi-angle polarization measurements by recursive fitting or optimization techniques using RT simulations of polarized light (Chowdhary, Cairns et al. 2001, Waquet, Cairns et al. 2009).

In this work, the approach is to use the spectrum of polarized light above the water to retrieve the spectrum of the attenuation coefficient c_{sol} of suspended matter, from which microphysical properties of this matter can be extracted (Twardowski, Boss et al. 2001). From the retrieval of the spectral attenuation coefficient of suspended particulate matter, the slope of the PSD can be approximated as follows (Hulst 1981):

$$c_{sol}(\lambda) = A\lambda^{-Y}, \tag{11}$$

where Y is the hyperbolic (power law) slope of the hydrosol's spectral attenuation and A is the amplitude. We obtain Y from c_{sol} (λ=440) and c_{sol} (λ=665) using

$$Y = \frac{\log[c_{sol}(440)/c_{sol}(665)]}{\log[665/440]} \tag{12}$$

Since the slope of the spectral attenuation Y (assuming it follows a power law) is closely related to the slope ξ of the PSD for a polydisperse hydrosols, it can be approximated as follows (Hulst 1981)

$$\xi = Y + 3 \tag{13}$$

A corrected model of Eq. 13 has been suggested by Boss *et* al. (2001) for cases where larger sized particles are more significant (Boss, Pegau et al. 2001, Boss, Twardowski et al. 2001).

The retrieval of PSD is therefore possible using Eq.s 12 and 13 provided that the hydrosol attenuation coefficient is well estimated. Our algorithms discussed in *Section* 4.3.1 allow for the retrieval of the total attenuation coefficient c as long as the total absorption coefficient a is known. The total absorption and attenuation coefficients include contributions from water, CDOM, and hydrosols (phytoplankton and NAP matter). Since the water properties are known in our modeling, they can be easily subtracted from c and a. This leaves CDOM absorption to be subtracted from c and a. In coastal waters that are highly affected by the CDOM, ignoring CDOM absorption can lead to an overestimation in the slope of the PSD (*i.e.* falsely indicating that the water contains higher densities of smaller particles) due to the high absorption at 440 nm. Several inversion algorithms that retrieve the CDOM absorption coefficient in coastal waters can be used in this inversion scheme (Lee, Carder et al. 2002, Ioannou, Gilerson et al. 2011).

To retrieve the bulk refractive index n_{bulk} of the water body, we use an analytical model based on the Mie theory developed by Twardowski *et al*. (2001) (Twardowski, Boss et al. 2001). This model predicts the bulk ocean particulate refractive index n_{bulk} from *Y* as follows:

$$n_{bulk}\left(\widetilde{b_b}_{sol}, Y\right) = 1 + \widetilde{b_b}_{sol}^{\,0.5377+0.4867(Y^2)}\left[1.4676 + 2.2950(Y^2) + 2.3113(Y^4)\right], \tag{14}$$

where $\tilde{b}_{b_{sol}}$ is the backscattering ratio of hydrosols defined as

$$\widetilde{b_b}_{sol} = \frac{b_{b_{sol}}}{b_{sol}} \quad . \tag{15}$$

In Eq. 15, backscattering coefficient $b_{b_{sol}}$ can be estimated using the QAA (Lee, Carder et al. 2002) method and hydrosol scattering coefficient b_{sol} can be obtained from $b_{sol} = c_{sol} - a_{sol}$.

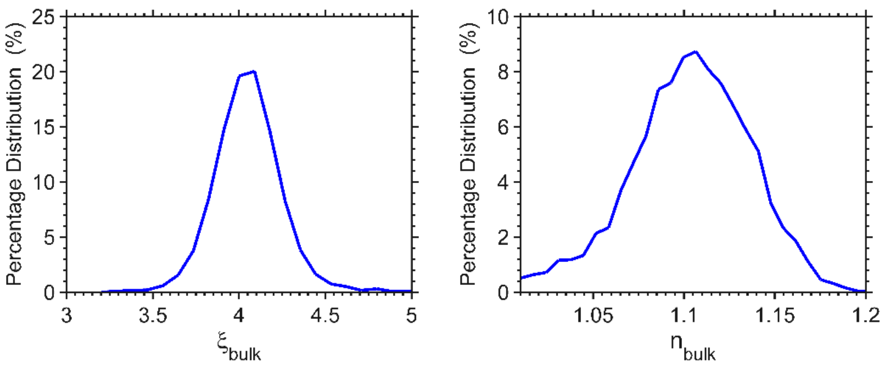

Figure 11. Histogram of the retrieval of the bulk refractive index n_{bulk} and the slope of the bulk PSD ξ_{bulk} from simulated DoLP^{0+} measurements.

Figure 11 shows the retrieval of the microphysical parameters based on Eq. 11-15. The main inputs to the inversion was the DoLP^{0+} at a 40° viewing angle above water and 90° azimuth angle relative to the Sun at 440 and 665 nm. After the inversion of the hydrosol attenuation coefficient and given the total and CDOM absorption coefficients at 440 and 665 nm, the slope of the particulate attenuation coefficient was calculated as in Eq. 12 and then ξ_{bulk} is calculated as in

Eq. (13). Based on the knowledge of the backscattering ratio given by Eq. 15, the bulk refractive index n_{bulk} is then calculated from Eq. 14. As shown in Figure 11, the ranges of the retrieved microphysical parameters are within the typical ranges for natural oceanic waters (Twardowski, Boss et al. 2001).

5. Validation results for the inversion algorithm against field measurements

5.1 RT simulations at 1 meter below the water surface

We validate the inversion algorithm discussed in *Section* 4.3.1 using field measurements by an underwater polarimeters (Tonizzo, Zhou et al. 2009). In order to carry out such validation, another set of the fitting coefficients for the inversion algorithm is used to retrieve the attenuation coefficient. Based on the RT simulation for the same IOPs described in *Section* 3.2, the DoLPs were obtained at 1 meter below the sea surface. The reason for the 1-meter depth is that the flotation system and geometry of the polarimeter design constrained it to measurements at depths of 1 meter or more below the air-water interface.

Figure 12 shows the relationship between the simulated DoLP at 1 meter below surface ($DoLP^{1m}$) and the *c/a* ratio for three wavelengths at Sun zenith angles 30° and 50°, at 90° relative azimuth angle, and at 40° in-water viewing zenith angle. That relationship is fitted with the third-order polynomial, shown in the figure in red lines. The variability in the relationship is similar to the $DoLP^{0-}$ just below the sea surface, though $DoLP^{1m}$ exhibits lower values because of the increase in multiple scattered light at 1 me below.

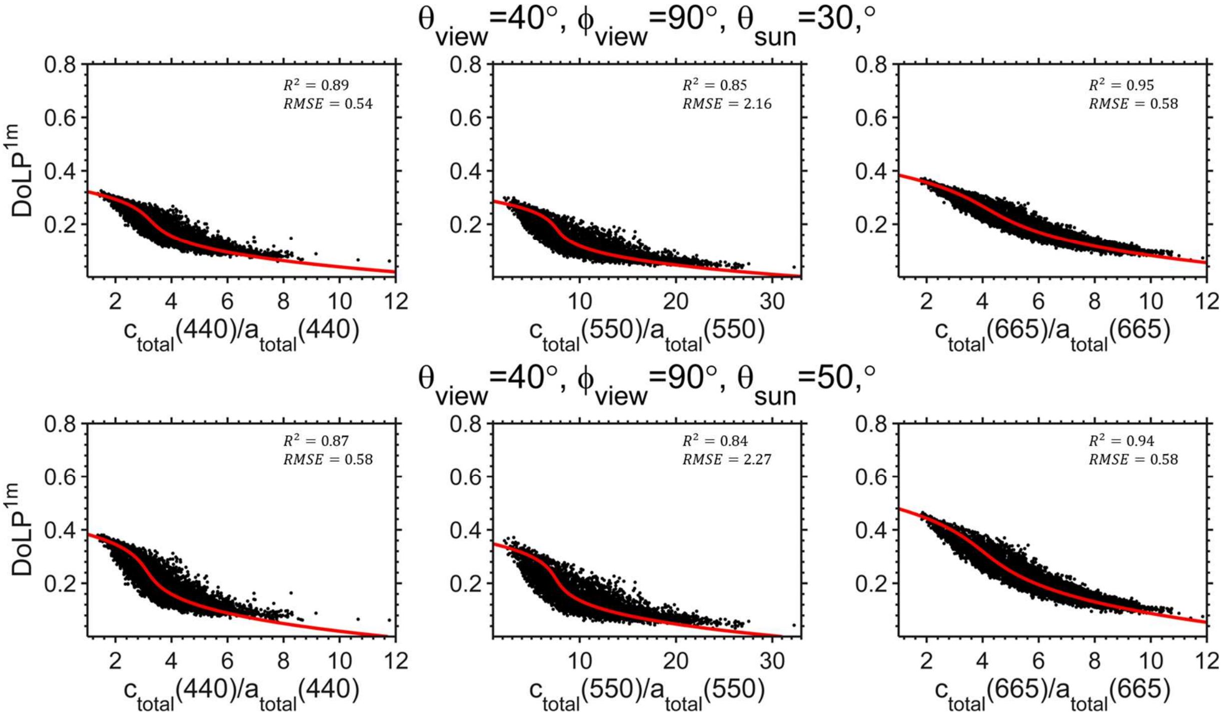

Figure 12. Fitted relationship between the DoLP at 1 m below the sea surface and c/a ratio at three wavelengths at θ_{view} = 40°, φ_{view} = 90° and θ_{sun} = 30° (θ_{sca} = 135.6°) (first row) and 50° (θ_{sca} = 128.4°) (second row).

5.2. Measurements and instrumentation

In order to measure the underwater polarization of light, a hyperspectral, multi-angular polarimeter was developed by the Optical Remote Sensing Laboratory at the City College of New York, NY shown underwater in Figure 14 (Tonizzo, Zhou et al. 2009, Gu, Carrizo et al. 2016).

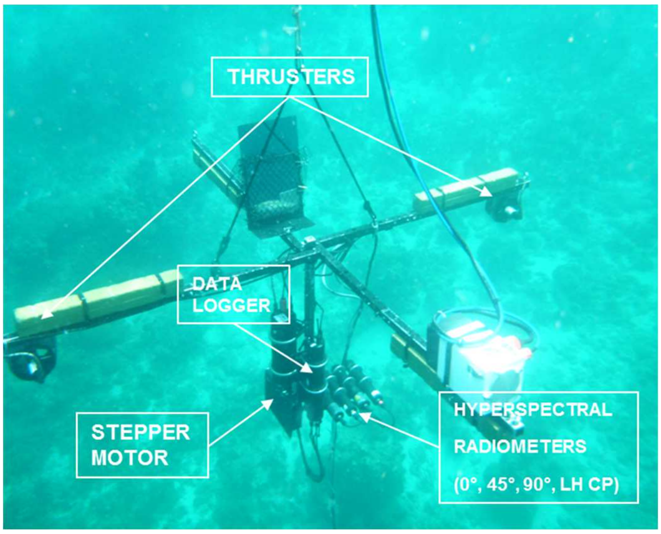

Figure 13. The underwater polarimeter deployed to measure the polarization of light in-water.

The instrument consists of three Satlantic Hyperspectral radiance sensors recording intensity over 350 – 800 nm wavelength range, with a 8.5º in–water field of view and mounted on a scanning system controlled by an underwater electric stepper motor (Newmark Systems, Inc.). Its three hyperspectral radiance sensors (HyperOCRs, Satlantic) each receive light through a linear polarizer (Edmund Optics) set to a specific angle: 0°, 45°, and 90° with respect to a reference axis. At this point, one should be careful not to confuse the angles used in describing the geometry of the polarimeter. While the relative angles of the linear polarizers fronting the radiometers are held fixed, the whole radiometer system can be rotated over a full circle of viewing angles. To distinguish these angles from the conventional viewing and viewing azimuth angles, they are henceforth referred to as *instrument* angles. Figure 14 clarifies the distinction. The stepper motor achieves zenith-viewing rotation in the vertical plane for the upwelling and downwelling light. The whole polarimeter assembly uses a pair of remotely controlled thrusters to achieve azimuth rotation and to perform measurements within the Sun principal plane or at angles with respect to it. Additional details about this instrument are available in Tonizzo *et al.* (2011) (Tonizzo, Gilerson et al. 2011).

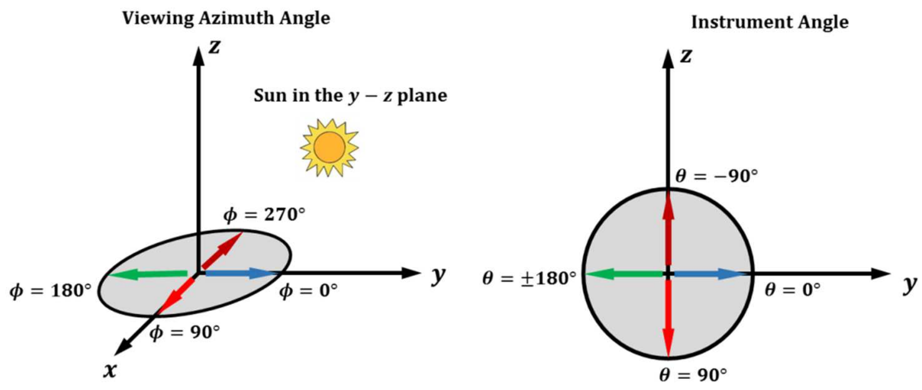

Figure 14. Definition of the viewing azimuth angle and the polarimeter's instrument angle.

The IOPs of the water body include the absorption and scattering coefficients of the particulates, and dissolved matter. The absorption and attenuation coefficients were measured hyperspectrally in the visible spectrum using the ac-s (WET Labs) instrument. The ac-s has two operating configurations: one measures the total absorption coefficients of both particulates and dissolved substances, and the other filters the water intake with a 0.2 μm filter pores to pass through and to measure only CDOM. The ac-s samples the IOPs over the depth profile of the water column. The operations of the instrument were directed towards performing sampling at different locations and water conditions.

5.3. Retrieval of the attenuation coefficient *c*

Since the summer of 2008, dozens of field measurements were collected at different stations using the underwater polarimeter and the WET Labs in-situ instrument package. The data points were collected at different locations near the northeastern coast of the US. The optical properties of the water varied but were within the conditions typical of coastal waters. Table 2 shows the geo-location of the stations used in the validation study.

Table 2. The stations used in the validation study.

STATIO N NO.	DATE	LOCATION	SUN ZENITH	RELATIVE AZIMUTH	RANGE OF SCATTERING ANGLES (in-water)
ST 1	21-Jul-08	New Jersey Bight	30°	0°	77°-158°
ST 2	21-Jul-08	New Jersey Bight	45°	0°	68°-145°
ST 3	22-Jul-08	New Jersey Bight	40°	10°	72°-151°
ST 4	23-Jul-08	New Jersey Bight	40	0°	71°-151°
ST 5	4-Aug-08	Rockaway Inlet, NY	25°	0°	82°-162°
ST 6	4-Aug-08	Rockaway Inlet, NY	30°	20°	79°-158°
ST 7	9-Jul-09	New York Harbor, NY	20°	0°	85°-165°
ST 8	9-Jul-09	New York Harbor, NY	20°	30°	87°-165°
ST 9	9-Jul-09	New York Harbor, NY	20°	10°	85°-165°
ST 10	9-Jul-09	New York Harbor, NY	20°	30°	87°-165°
ST 11	9-Jul-09	New York Harbor, NY	25°	50°	88°-162°
ST 12	19-Aug-10	Proximate to LISCO*	35°	90°	99°-155°
ST 13	19-Aug-10	Proximate to LISCO	25°	10°	82°-162°
ST 14	19-Aug-10	Proximate to LISCO	30°	90°	99°-158°
ST 15	19-Aug-10	Proximate to LISCO	30°	90°	99°-158°

*Long Island Sound Coastal Observatory, part of AERONET-OC network (Harmel, Gilerson et al. 2011)

Table 2 shows that in-situ measurements were performed at different Sun illumination and viewing geometries. These stations passed quality control tests to reduce the environmental effects that can impact the in-situ optical measurements, such as limiting wind speed to 5 m/s and choosing stations with clear skies. The underwater polarimeter measured the polarized light with a full scan of the upwelling light at 1 m below the surface. At this depth, surface effects on the upwelling light are minimized, but the wind speed is limited to ensure that the apparatus is stable enough in the upright vertical position to reduce tilt biases.

The in-situ measurements of the attenuation and absorption coefficients are shown in Figure 15 and cover a broad range of water conditions.

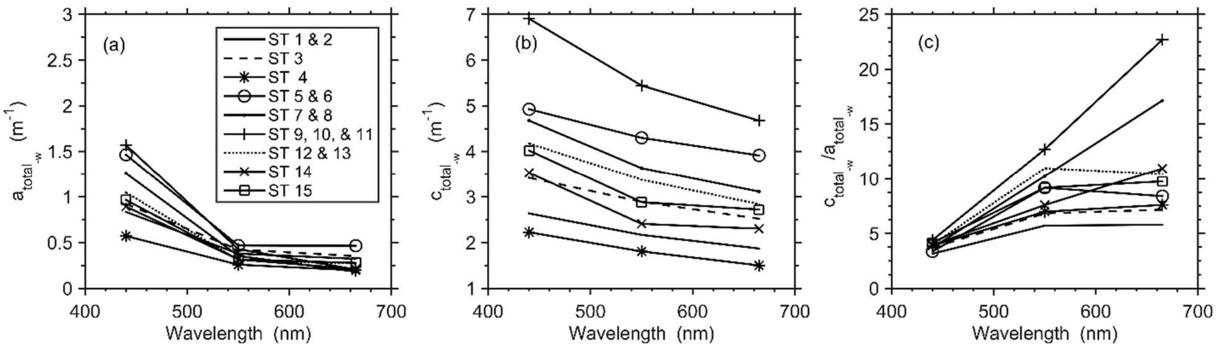

Figure 15. Total absorption, (a), attenuation, (b), coefficients and their ratios, (c), without the pure water component at 440, 550, and 665 nm for 15 stations.

The absorption and attenuation coefficients displayed in Figure 15 do not include contributions from pure sea water, and are therefore denoted with the subscript "-*w*" to differentiate them from coefficients that include the sea water contribution. The variability of the coefficients as well as the *c*/*a* ratio is for typical moderately turbid coastal waters. The lowest variability of *c*/*a* ratio is at 440 nm, while its highest is at 665 nm. By adding the high absorption of the water component, the range of the variability of the ratio becomes smaller. These observations matches the theoretical IOPs modeling used in the VRT simulations.

Figure 16 shows the DoLP at 1 m below the sea surface measured using the underwater polarimeter. The DoLP were calculated from the Stokes components of the linearly polarized light measured by the three radiometers as described in *Section* 5.2.

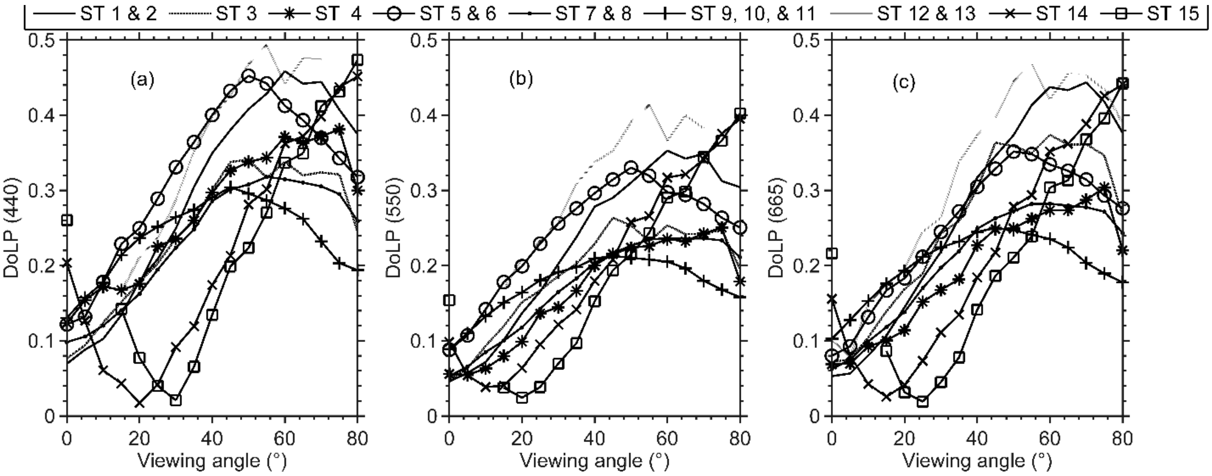

Figure 16. DoLP versus viewing angle (as defined in Figure 5) at 1 m below at 440, 550, and 665 nm (a), (b), and (c), respectively for 15 stations. (0° viewing angle is when the detector is looking at the nadir).

The fact that DoLP is not as smooth as the RT simulations predict is due to either radiometric uncertainties in the polarimeter or to other environmental factors (Tonizzo, Zhou et al. 2009). The uncertainties of the measurements could be high because of the low upwelling light signal at 1 m below the surface, especially for turbid coastal waters and in the red part of the spectrum, where the light is highly attenuated (due to water absorption) as shown in Figure 15. The uncertainties also can increase for specific geometries such as the nadir direction where the radiances are minimal and the DoLP is low in the near backscattering directions (*i.e.* $\theta \sim 180°$). The spectral variations of the DoLP are similar to the RayXP simulations predictions, where DoLP at 440 and 665 nm exhibits higher values than at 550 nm. That is due to the increase of the total absorption coefficients at the blue and red wavelengths reducing multiple scattering, while in the green, the absorption is minimal, and increased multiple scattering occurs. Therefore, the absorption of light by hydrosols has a modulating effect on the polarization of light with respect to baseline Rayleigh-like scattering and hydrosols scattering themselves.

Based on the DoLP measurements in Figure 16, it is possible to retrieve the ratio between the attenuation and absorption coefficients (*c*/*a*) using the polynomial coefficients from *Section* 4.3.1 for a given geometry of viewing, Sun zenith, and relative azimuth angle. After applying the polynomial function from Eq. 8 to retrieve *c*/*a*, the ratio is then multiplied by the total absorption coefficient (including water) measured by the ac-s instrument shown in Figure 15(a). The retrieved total attenuation coefficient from the DoLP is then compared to the total attenuation coefficient (after adding the water component) measured by the ac-s instrument. A scatter plot of the retrieval of the attenuation coefficient based on the DoLP measurements is shown in Figure 17 where the coefficients were averaged over the viewing angles from 40° to 80°.

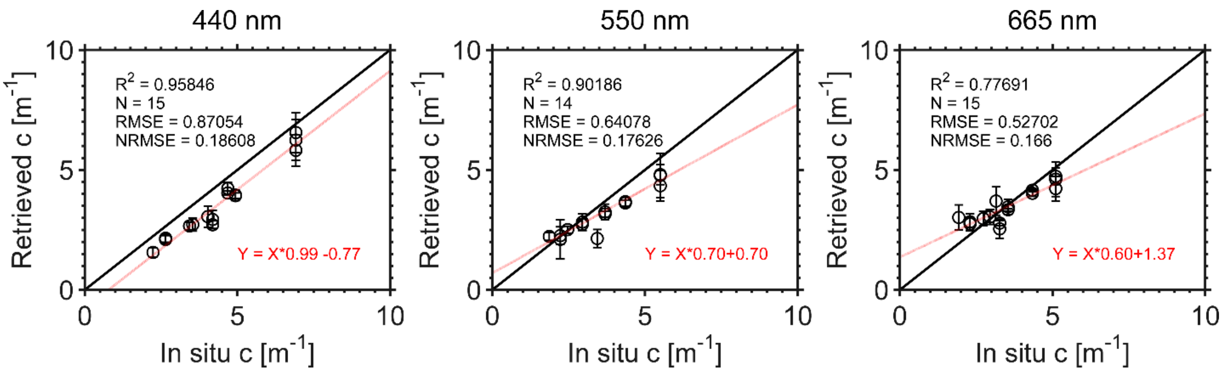

Figure 17. The retrieval of the total attenuation coefficient averaged over different viewing angles from 40° to 80° and the standard deviation represented as the error bars for three wavelengths.

In Figure 17, the coefficient of determination R^2 is greater than 0.9 for both the 440 and 550 nm, while it degrades for the 665 nm. The root-mean-square error (RMSE) and normalized root-mean-square error (NRMSE) values at 665 nm are lower than at 440 and 550 nm, indicating lower error in the retrieval at the 665 nm, while the decreased correlation is due to the reduction in the dynamic range of the attenuation coefficient, where it is typically lower at the red part of the spectrum. Additionally, the number of available stations is limited; therefore, outliers can strongly affect the correlation indicators. At 665 nm, the correlation decreases at geometries where the polarimeter is looking in the nadir direction, as the upwelling radiance is small due to the absorptive nature of the water in that part of the spectrum.

Figure 18 shows the retrieval of *c* from the DoLP measured at 75° viewing angle. The R^2 values are very good for the three wavelengths, where the highest value is at the 440 nm, while the lowest NRMSE is at the 665 nm.

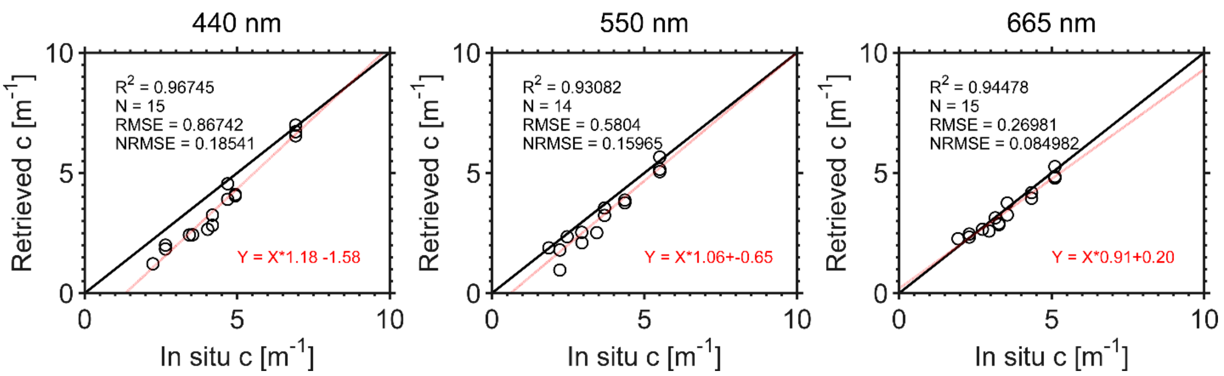

Figure 18. The retrieval of the total attenuation coefficient for 75° viewing angle for three wavelengths.

In both Figures 17 and 18, the red lines show the linear regression between the in-situ and the retrieved *c*. The slope and bias in all the cases might be due to multiple sources of error, such as radiometric uncertainties, which play a major role in introducing differences between retrieved and measured in-situ values. For example, at the cases where the attenuation coefficient increases, the radiometric uncertainties of the polarimeters increase as well due to the decrease in the measured DoLP. Therefore, the retrieval of *c* in turbid waters could be more challenging due to signal to noise ratio limitations. Meanwhile, the in-situ measurements might also introduce a slope as a result of calibration errors of the ac-s instrument (Mckee, Piskozub et al. 2008). The inverse model itself also might introduce some of the uncertainties in the retrieval because of the inadequacy either of the bio-optical model, or in the polynomial fitting function that does not produce a high quality fit. While investigating of such problems (*i.e.* calibration and modeling) is necessary, due to the lack of in-situ measurements of the DoLP and the IOPs at the appropriate environmental and illumination/viewing geometries, and the lack of microphysical properties of the ocean (*i.e.*, refractive index and PSD) that reproduces the scattering matrix of the polarized light used in the hybrid bio-optical model, this work should be revisited when such data are more available within the ocean color community.

6. Remote sensing application

Remote sensing algorithms for ocean color retrievals from satellite measurements require atmospheric correction of the top of atmosphere (TOA) radiance. From scalar satellite TOA measurements, AC algorithm removes the contribution of atmospheric path radiance (*i.e.* Rayleigh, and aerosol scattering) and compensates for gaseous absorption in the atmosphere, as well as ocean surface glint. These effects typically are pre-computed using a fully coupled radiative transfer simulations for pre-determined aerosol models, optical thicknesses, and geometries. The residual signal is the ocean contribution to derive ocean color products such as chlorophyll concentration and IOPs. Likewise, polarimetric remote sensing algorithms will require adequate knowledge of the atmospheric effects on the TOA polarimetric signal. The TOA polarized signature is largely attributed to the single scattering of light by the mix of aerosol particles and atmospheric molecules (Hansen and Travis 1974, Mishchenko, Cairns et al. 2007, Chowdhary, Cairns et al. 2012). To understand the impact of the atmosphere on the polarized signature of the ocean emerging at the TOA, we simulated 5000 cases of coastal waters and analyzed the sensitivity of the relationship between $DoLP^{TOA}$ and *c/a* ratio for clear and highly turbid atmosphere (*i.e.,* $\tau(400\ nm)$ = 0.1 and 0.7, respectively). Since the TOA signal's main contribution is from the atmosphere (with fixed optical properties of the continental aerosol model), while the signal from the oceanic layer with varying optical parameters is to be assessed, we performed a sensitivity analysis by calculating the dynamic range (DR^{TOA}) of the $DoLP^{TOA}$ for all possible viewing geometry at the TOA. DR for the 5000 cases of oceanic layer is calculated as follows:

$$DR^{TOA} = \frac{\max(DoLP^{TOA})}{\min(DoLP^{TOA})}, \tag{16}$$

where the DR^{TOA} change is ≥ 1. Higher DR signifies higher variability in the $DoLP^{TOA}$ versus *c/a* ratio and therefore a larger impact of the ocean signal at the TOA.

Figures 19 is the synoptic polar plots of the DR^{TOA} for three wavelengths and at Sun zenith angle $\theta_{sun} = 30°$ for $\boldsymbol{\tau} =$ 0.1 and 0.7. Of note, the 440 nm channel shows a low DR which can be accounted for by the high contribution of the atmospheric molecular and aerosols scattering. Conversely, DR^{TOA} at 550 and 665 nm is much higher, reaching more than 3, depending on the viewing, Sun geometry and AOT. Higher DR does not necessarily allow a better retrieval of the ocean parameters. Two conditions should be satisfied to allow retrieval at the TOA: 1) the DR is large enough to allow the measurements of Stokes components with low radiometric uncertainties at the TOA, and 2) there must be a definitive relationship between DoLP and *c/a*. Therefore, the use of a single viewing geometry for the retrieval needs to be carefully assessed for possible illumination scenarios and atmospheric conditions.

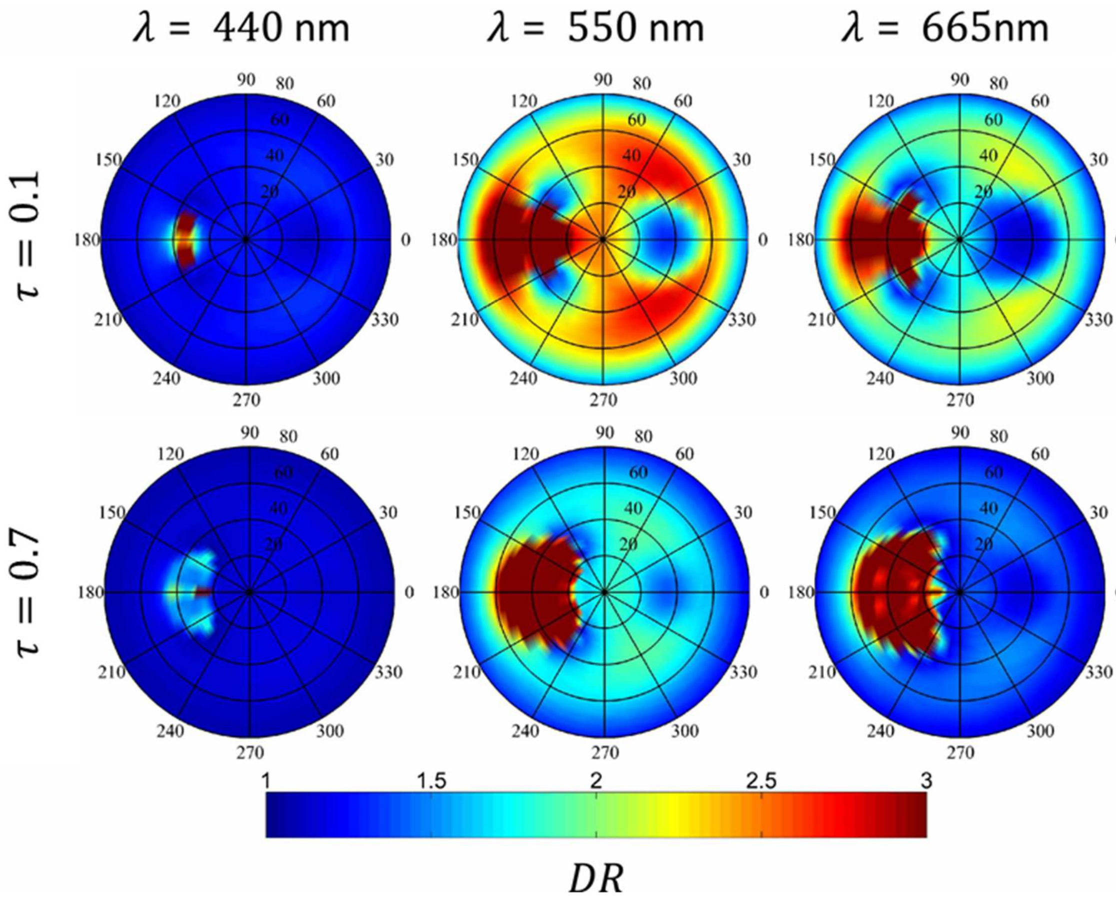

Figure 19. Synoptic polar plot of the Dynamic Range (DR) calculated for τ = 0.1 and 0.7, and for Sun zenith 30° at 440, 550, and 665 nm.

Increasing AOT leads to degradation of the relationship between DoLP and *c/a* ratio. The DR decreases dramatically for all wavelengths and viewing/illumination geometry. The polarized signature of the atmosphere masks the influence of the hydrosols on the degree of polarization at the TOA. The highly turbid atmosphere scenario cannot allow the retrieval of the *c/a* ratio.

The high DR regions in the polar plots are in the backscattering direction where the light is completely or highly unpolarized. At such geometry, there is no relationship between the DoLP in water and the *c/a* ratio. Therefore, the high DR is likely due to the fact that both numerator and denominator values of DR are close to zero, which thus induces meaningless values of the ratio DR.

In the next figure, we show the scatter plot between $DoLP^{TOA}$ and *c/a* at 40° viewing zenith angle and 90° and 60° viewing azimuth angle. The 60° azimuth angle shows a reasonable high DR of 2 and above.

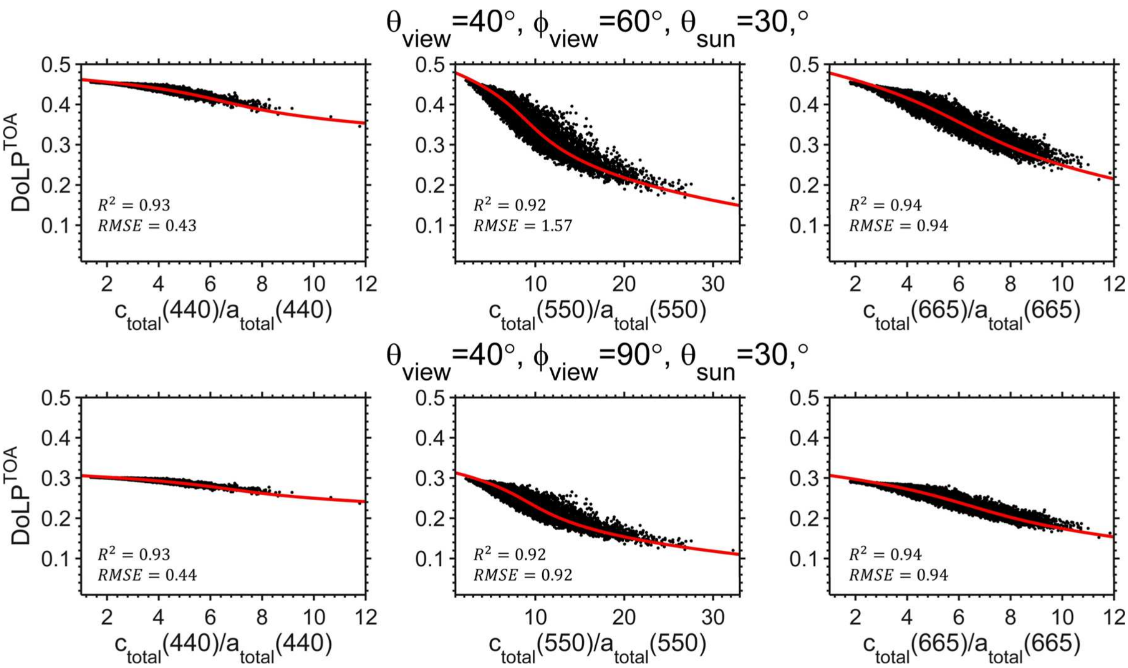

Figure 20. The relation between $DoLP^{TOA}$, simulated for τ = 0.1, and c/a at the TOA at three wavelengths, at 40° viewing zenith angle and for Sun relative azimuth angle of 90° and 60°. Sun zenith angle is fixed at 30°. (θ_{sca} = 120.2°) (first row) and 50° (θ_{sca} = 131.5°) (second row).

In Figure 20, there is a distinctive relationship at all three wavelengths and at the two viewing geometry when τ = 0.1. At 440 nm, the DR of the $DoLP^{TOA}$ is very small, making it more difficult to retrieve ocean's optical properties, whereas at 550 and 665 nm, the DR is much higher and the relationship between $DoLP^{TOA}$ and *c/a* is strong. The DR at 60° relative azimuth viewing angle is higher than at 90°. At 60° azimuth angle, the ocean signal can be contaminated by the Sun glint depending on the wind speed. Higher wind speed can lead to a higher contribution of the glint and therefore a contamination of the total signal at the TOA.

Figure 21 shows the same scatter plot as in Figure 20 but for $\tau = 0.7$. The turbid atmosphere, as expected, shows a lower DR while it retains the relationship between DoLP and *c/a*. The 440 nm channel shows a large degradation in the sensitivity due to the increasing aerosol's impact on the TOA signal. On the other hand, the relationship at the 550 nm is obvious especially at 60° azimuth angle. The 665 nm channel shows degradation in sensitivity, which could account for the weak polarized radiometric quantities that emerges from the ocean at the TOA.

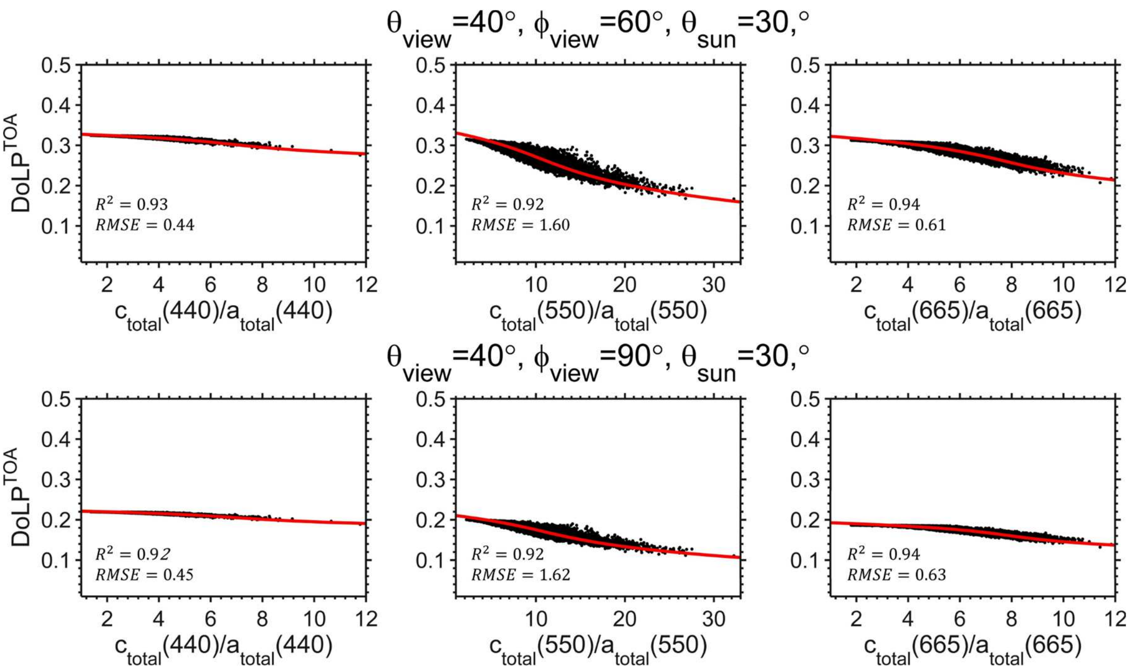

Figure 21. The relation between DoLP^{TOA}, simulated for τ = 0.7, and c/a at the TOA at three wavelengths, at 40° viewing zenith angle and for Sun relative azimuth angle of 90° and 60°. Sun zenith angle is fixed at 30° .(θ_{sca} = 120.2°) (first row) and 50° (θ_{sca} = 131.5°) (second row).

The synoptic polar plots in Figure 19 show that the 440 nm channel is a good channel for the retrieval of aerosol parameters due to the low contribution of the ocean polarized signature of

Case II water to the total signal at the TOA at all viewing geometry. The low DR is also apparent at the 550 and 665 nm channels in the principal plane and near it.

Based on the previous sensitivity analysis, the following recommendation can allow a future development of polarimetric ocean color retrieval from future polarimetric satellite missions:

1) TOA polarized light is weakly dependent on the polarized ocean contribution in the shorter wavelengths which corroborates with the results obtained by Chami (2007) (Chami 2007), thus allowing AC of the aerosols contribution in-conjunction with Near-infrared (NIR) AC algorithms.
2) Deriving the attenuation coefficient from $DoLP^{TOA}$ is possible at the green-red wavelength over coastal waters under a given specific geometry.
3) Based on this study, a single viewing geometry can allow retrieval of the attenuation coefficient for angle range $\theta_{view} = 40\,° \sim 70\,°$ and $\varphi_{view} = 30\,° \sim 90\,°$.

7. Conclusion

This work examines the development of an inversion methodology, which exploits the polarization properties of scattered light to retrieve optical and microphysical properties of oceanic waters. The theoretical modeling presented in this work encompasses a full characterization of the relationship between the DoLP and the ratio of attenuation/absorption coefficients (*c/a*). It is based on vector RT simulations performed for plane-parallel AO system, and examines the impact of different illumination/viewing geometry on the DoLP. An inverse algorithm is developed to retrieve the attenuation coefficient *c* at 440, 550, and 665 nm. Based on this retrieval, microphysical properties of hydrosols, such as the bulk refractive index and the PSD, can also be retrieved. The strong dependence of the polarization signature on multiple scattering permits parameterization of the relationship between DoLP and the concentration of in-organic mineral particles, [NAP], from which [NAP] at 665 nm can possibly be retrieved.

Two bio-optical models are developed to address, separately, the type and the optical variability of open (Case I) oceans and coastal (Case II) oceans. These models were used as inputs to the VRT program, RayXP, to simulate the Stokes components of light at just below the sea surface, which shows the strong dependency of the DoLP on the ratio of the attenuation/absorption coefficients (*c/a*) for Case II waters. An analytical third-order polynomial fit is then applied to parameterize this dependency, which, in turn, is used for the retrieval of the attenuation coefficient *c* at multiple illumination/viewing geometry. Retrievals with the parameterized relationship are assessed for uncertainties at the three wavelengths of the simulations showing R^2 values higher than 0.85 for most of the geometries (except in the backscattering direction). For above-water detection, the 90° azimuth angle and 40° viewing zenith angle is minimally affected by Sun glint, permitting easier corrections of surface glint effects in the upwelling polarized reflectance, while a strong relationship between DoLP and *c*/*a* still persist allowing the retrieval.

For this geometry, we also developed an inversion method to obtain the bulk refractive index and the PSD of hydrosols from the retrieved spectral attenuation coefficient at two wavelengths. This inversion approach obtains the slope of the Junge PSD from the slope of the particulate spectral attenuation coefficient. Then, following the approach developed by Twardowski *et al*. (Twardowski, Boss et al. 2001), the bulk refractive index of hydrosols can be retrieved given the backscattering ratio coefficient and the PSD.

Case I waters, as opposed to Case II waters, show a weaker relationship between DoLP and *c/a,* especially at 440 and 665 nm, because the polarized signal is masked by Rayleigh scattering in the blue channel and the high water absorption in the red channel. However, at 550 nm, there is a noticeable relationship for most of the viewing geometries, except for those near the backscattering direction. This is so because the phytoplankton particles are the dominant constituent in open water conditions, and DoLP becomes sensitive to their scattering coefficient in the green wavelength. In the solar half-principal plane, the relationship showed its maximum dynamic range or sensitivity. Several options are discussed for further possible applications of polarimetric observations and retrievals in Case I waters.

To validate our inversion approach, measurements of the DoLP with a custom-built underwater polarimeter are used for different water conditions and illumination/viewing geometries. Absorption and attenuation coefficients are measured at 1 meter below the sea surface, while a new parameterization for the relationship between DoLP and *c/a* was used to retrieve the attenuation coefficient *c*. The results show promising retrievals at the 440, 550, and 665 nm, although additional validation points are required to perform a more thorough validation analysis. The averaged DoLP measured over viewing angles ranging from 40° to 80° lead to retrievals with R^2 higher than 0.9 at 440 and 550 nm. This correlation degrades at 665 nm due to the limited variability of the attenuation coefficient at that wavelength, in addition to the limited number of validation points used, thus increasing impact of outliers. However, retrievals at 665 nm show NRMSE values similar to those at other wavelengths. The retrievals of *c* show improvements at the 75° viewing angle for the three wavelengths, with R^2 higher than 0.93. The NRMSE values are generally lower than 0.18 and can be as low as 0.08 for the 665 nm channel. This improvement in retrievals is due to the reduction in radiometric uncertainties and the physical stability of the polarimeter system when measuring underwater light.

The TOA preliminary sensitivity analysis of the $DoLP^{TOA}$ showed that it is possible to retrieve the attenuation coefficient using a single viewing geometry at the green-red wavelengths, while the $DoLP^{TOA}$ at 440 nm is mainly attributed to the atmospheric scattering, which can be used for the development of AC algorithms. A complete remote sensing algorithm needs to be developed for future satellite missions, such as PACE, 3MI, and GCOM-C, that will utilize polarimetric remote sensing. The work presented here can provide a starting point for the development of a pre-launch algorithm.

Acknowledgments

The Ocean Biology and Biochemistry Program of National Aeronautics and Space Administration (NASA), National Oceanic and Atmospheric Administration (NOAA), and the Office of Naval Research (ONR) funded this research. We acknowledge our thanks to Dr. Samantha Weltz and Amy Houghton for editorial efforts to improve the manuscript and the anonymous reviewers for their insightful remarks.

References

Ahmad, Z., et al. (2010). "New aerosol models for the retrieval of aerosol optical thickness and normalized water-leaving radiances from the SeaWiFS and MODIS sensors over coastal regions and open oceans." Applied Optics **49**(29): 5545-5560.

Babin, M., et al. (2003). "Light scattering properties of marine particles in coastal and open ocean waters as related to the particle mass concentration." Limnology and Oceanography **48**(2): 843-859.

Babin, M., et al. (2003). "Variations in the light absorption coefficients of phytoplankton, nonalgal particles, and dissolved organic matter in coastal waters around Europe." Journal of Geophysical Research-Oceans **108**(C7).

Behrenfeld, M. J. and E. Boss (2003). "The beam attenuation to chlorophyll ratio: an optical index of phytoplankton physiology in the surface ocean?" Deep-Sea Research Part I-Oceanographic Research Papers **50**(12): 1537-1549.

Behrenfeld, M. J., et al. (2005). "Carbon-based ocean productivity and phytoplankton physiology from space." Global Biogeochemical Cycles **19**(1).

Boss, E., et al. (2001). "Spectral particulate attenuation and particle size distribution in the bottom boundary layer of a continental shelf." Journal of Geophysical Research-Oceans **106**(C5): 9509-9516.

Boss, E., et al. (2001). "Shape of the particulate beam attenuation spectrum and its inversion to obtain the shape of the particulate size distribution." Applied Optics **40**(27): 4885-4893.

Bricaud, A., et al. (1998). "Variations of light absorption by suspended particles with chlorophyll a concentration in oceanic (case 1) waters: Analysis and implications for bio-optical models." Journal of Geophysical Research-Oceans **103**(C13): 31033-31044.

Carder, K. L., et al. (1999). "Semianalytic Moderate-Resolution Imaging Spectrometer algorithms for chlorophyll a and absorption with bio-optical domains based on nitrate-depletion temperatures." Journal of Geophysical Research-Oceans **104**(C3): 5403-5421.

Cetinic, I., et al. (2012). "Particulate organic carbon and inherent optical properties during 2008 North Atlantic Bloom Experiment." Journal of Geophysical Research-Oceans **117**.

Chami, M. (2007). "Importance of the polarization in the retrieval of oceanic constituents from the remote sensing reflectance." Journal of Geophysical Research-Oceans **112**(C5).

Chami, M. and D. Mckee (2007). "Determination of biogeochemical properties of marine particles using above water measurements of the degree of polarization at the Brewster angle." Optics Express **15**(15): 9494-9509.

Chami, M. and M. D. Platel (2007). "Sensitivity of the retrieval of the inherent optical properties of marine particles in coastal waters to the directional variations and the polarization of the reflectance." Journal of Geophysical Research-Oceans **112**(C5).

Chami, M., et al. (2001). "Radiative transfer model for the computation of radiance and polarization in an ocean-atmosphere system: polarization properties of suspended matter for remote sensing." Applied Optics **40**(15): 2398-2416.

Chowdhary, J. (1999). "Multiple Scattering of Polarized Light in Atmosphere-Ocean Systems: Application to Sensitivity Analyses of Aerosol Polarimetry." Ph.D. thesis. Columbia University.

Chowdhary, J., et al. (2001). "Retrieval of aerosol properties over the ocean using multispectral and multiangle photopolarimetric measurements from the Research Scanning Polarimeter." Geophysical Research Letters **28**(2): 243-246.

Chowdhary, J., et al. (2006). "Contribution of water-leaving radiances to multiangle, multispectral polarimetric observations over the open ocean: bio-optical model results for case 1 waters." Applied Optics **45**(22): 5542-5567.

Chowdhary, J., et al. (2012). "Sensitivity of multiangle, multispectral polarimetric remote sensing over open oceans to water-leaving radiance: Analyses of RSP data acquired during the MILAGRO campaign." Remote Sensing of Environment **118**: 284-308.

Ciotti, A. M., et al. (2002). "Assessment of the relationships between dominant cell size in natural phytoplankton communities and the spectral shape of the absorption coefficient." Limnology and Oceanography **47**(2): 404-417.

Cox, C. and W. H. Munk (1956). Slopes of the sea surface deduced from photographs of sun glitter. Berkeley,, University of California Press.

Doxaran, D., et al. (2009). "Spectral variations of light scattering by marine particles in coastal waters, from visible to near infrared." Limnology and Oceanography **54**(4): 1257-1271.

Gilerson, A., et al. (2007). "Fluorescence component in the reflectance spectra from coastal waters. Dependence on water composition." Optics Express **15**(24): 15702-15721.

Gordon, H. R. (1989). "Can the Lambert-Beer Law Be Applied to the Diffuse Attenuation Coefficient of Ocean Water." Limnology and Oceanography **34**(8): 1389-1409.

Gordon, H. R., et al. (1988). "A Semianalytic Radiance Model of Ocean Color." Journal of Geophysical Research-Atmospheres **93**(D9): 10909-10924.

Gordon, H. R., et al. (1975). "Computed Relationships between Inherent and Apparent Optical-Properties of a Flat Homogeneous Ocean." Applied Optics **14**(2): 417-427.

Gordon, H. R., et al. (1983). Remote Assessment of Ocean Color for Interpretation of Satellite Visible Imagery A Review. Lecture Notes on Coastal and Estuarine Studies,. New York, NY, Springer US,.

Goyens, C., et al. (2013). "Evaluation of four atmospheric correction algorithms for MODIS-Aqua images over contrasted coastal waters." Remote Sensing of Environment **131**: 63-75.

Graff, J. R., et al. (2015). "Analytical phytoplankton carbon measurements spanning diverse ecosystems." Deep-Sea Research Part I-Oceanographic Research Papers **102**: 16-25.

Gu, Y., et al. (2016). "Polarimetric imaging and retrieval of target polarization characteristics in underwater environment." Applied Optics **55**(3): 626-637.

Hansen, J. E. and L. D. Travis (1974). "Light-Scattering in Planetary Atmospheres." Space Science Reviews **16**(4): 527-610.

Harmel, T. and M. Chami (2008). "Invariance of polarized reflectance measured at the top of atmosphere by PARASOL satellite instrument in the visible range with marine constituents in open ocean waters." Optics Express **16**(9): 6064-6080.

Harmel, T. and M. Chami (2012). "Determination of sea surface wind speed using the polarimetric and multidirectional properties of satellite measurements in visible bands." Geophysical Research Letters **39**.

Harmel, T., et al. (2011). "Long Island Sound Coastal Observatory: Assessment of above-water radiometric measurement uncertainties using collocated multi and hyperspectral systems." Applied Optics **50**(30): 5842-5860.

Honda, Y., et al. (2006). "The possibility of SGLI/GCOM-C for Global environment change monitoring." Sensors, Systems, and Next-Generation Satellites X **6361**: U41-U44.

Hulst, H. C. v. d. (1981). Light scattering by small particles. New York, Dover Publications.

Ibrahim, A., et al. (2012). "The relationship between upwelling underwater polarization and attenuation/absorption ratio." Optics Express **20**(23): 25662-25680.

Ioannou, I., et al. (2011). "Neural network approach to retrieve the inherent optical properties of the ocean from observations of MODIS." Applied Optics **50**(19): 3168-3186.

IOCCG (2006). "Remote Sensing of Inherent Optical Properties: Fundamentals,Tests of Algorithms, and Applications."

Kattawar, G. W. and C. N. Adams (1989). "Stokes Vector Calculations of the Submarine Light-Field in an Atmosphere-Ocean with Scattering According to a Rayleigh Phase Matrix - Effect of Interface Refractive-Index on Radiance and Polarization." Limnology and Oceanography **34**(8): 1453-1472.

Kattawar, G. W., et al. (1973). "Explicit Form of Mie Phase Matrix for Multiple Scattering Calculations in I, Q, U and V Representation." Journal of the Atmospheric Sciences **30**(2): 289-295.

Knobelspiesse, K., et al. (2011). "Simultaneous retrieval of aerosol and cloud properties during the MILAGRO field campaign." Atmospheric Chemistry and Physics **11**(13): 6245-6263.

Lee, Z. P., et al. (2002). "Deriving inherent optical properties from water color: a multiband quasi-analytical algorithm for optically deep waters." Applied Optics **41**(27): 5755-5772.

Loisel, H., et al. (2008). "Investigation of the variations in the water leaving polarized reflectance from the POLDER satellite data over two biogeochemical contrasted oceanic areas." Optics Express **16**(17): 12905-12918.

Lotsberg, J. K. and J. J. Stamnes (2010). "Impact of particulate oceanic composition on the radiance and polarization of underwater and backscattered light." Optics Express **18**(10): 10432-10445.

Marbach, T., et al. (2015). "The 3MI Mission: Multi-Viewing -Channel -Polarisation Imager of the EUMETSAT Polar System: Second Generation (EPS-SG) dedicated to aerosol and cloud monitoring." Polarization Science and Remote Sensing Vii **9613**.

Mckee, D., et al. (2008). "Scattering error corrections for in situ absorption and attenuation measurements." Optics Express **16**(24): 19480-19492.

Mishchenko, M. I. Electromagnetic scattering by particles and particle groups : an introduction.

Mishchenko, M. I., et al. (2004). "Monitoring of aerosol forcing of climate from space: analysis of measurement requirements." Journal of Quantitative Spectroscopy & Radiative Transfer **88**(1-3): 149-161.

Mishchenko, M. I., et al. (2007). "Accurate monitoring of terrestrial aerosols and total solar irradiance - Introducing the glory mission." Bulletin of the American Meteorological Society **88**(5): 677-+.

Mishchenko, M. I., et al. (2002). Scattering, absorption, and emission of light by small particles. Cambridge ; New York, Cambridge University Press.

Mobley, C. D. and L. K. Sundman (2008). HYDROLIGHT 5: Technical documentation. Sequoia Scientific, Inc.

Morel, A. (1974). "Optical properties of pure water and pure sea water." Optical Aspects of Oceanography, N. G. Jerlov, and E. S. Nielsen, eds. (Academic Press, New York, 1974), pp. 1-24.

Morel, A., et al. (2002). "Bidirectional reflectance of oceanic waters: accounting for Raman emission and varying particle scattering phase function." Applied Optics **41**(30): 6289-6306.

Morel, A. and S. Maritorena (2001). "Bio-optical properties of oceanic waters: A reappraisal." Journal of Geophysical Research-Oceans **106**(C4): 7163-7180.

PACE (2012). "Pre-Aerosol, Clouds, and ocean Ecosystem (PACE) Mission Science Definition Team Report."

Pope, R. M. and E. S. Fry (1997). "Absorption spectrum (380-700 nm) of pure water .2. Integrating cavity measurements." Applied Optics **36**(33): 8710-8723.

Stramski, D., et al. (2001). "Modeling the inherent optical properties of the ocean based on the detailed composition of the planktonic community." Applied Optics **40**(18): 2929-2945.

Timofeyeva, V. A. (1970). "Degree of polarization of light in turbid media." Izvestiya Akademii Nauk Sssr Fizika Atmosfery. I. Okeana **6**(513–522).

Tonizzo, A., et al. (2011). "Estimating particle composition and size distribution from polarized water-leaving radiance." Applied Optics **50**(25): 5047-5058.

Tonizzo, A., et al. (2009). "Polarized light in coastal waters: hyperspectral and multiangular analysis." Optics Express **17**(7): 5666-5682.

Twardowski, M. S., et al. (2001). "A model for estimating bulk refractive index from the optical backscattering ratio and the implications for understanding particle composition in case I and case II waters." Journal of Geophysical Research-Oceans **106**(C7): 14129-14142.

Tynes, H. H., et al. (2001). "Monte Carlo and multicomponent approximation methods for vector radiative transfer by use of effective Mueller matrix calculations." Applied Optics **40**(3): 400-412.

Voss, K. J. and E. S. Fry (1984). "Measurement of the Mueller Matrix for Ocean Water." Applied Optics **23**(23): 4427-4439.

Waquet, F., et al. (2009). "Polarimetric remote sensing of aerosols over land." Journal of Geophysical Research-Atmospheres **114**.

Wozniak, S. B. and D. Stramski (2004). "Modeling the optical properties of mineral particles suspended in seawater and their influence on ocean reflectance and chlorophyll estimation from remote sensing algorithms." Appl Opt **43**(17): 3489-3503.

You, Y., et al. (2011). "Polarized light field under dynamic ocean surfaces: Numerical modeling compared with measurements." Journal of Geophysical Research-Oceans **116**.

You, Y., et al. (2011). "Measurements and simulations of polarization states of underwater light in clear oceanic waters." Applied Optics **50**(24): 4873-4893.

Young, A. T. (1980). "Revised Depolarization Corrections for Atmospheric Extinction." Applied Optics **19**(20): 3427-3428.

Zege, E. P., et al. (1993). "Multicomponent Approach to Light-Propagation in Clouds and Mists." Applied Optics **32**(15): 2803-2812.